1998

Characterizing Enso with Nonlinear Dynamics

Corrie Modell Aljain
University of Rhode Island

CHARACTERIZING ENSO
WITH NONLINEAR DYNAMICS

BY

CORRIE MODELL ALJIAN

A THESIS SUBMITTED IN PARTIAL FULFILLMENT OF THE
REQUIREMENTS FOR THE DEGREE OF
MASTER OF SCIENCE
IN
OCEANOGRAPHY

UNIVERSITY OF RHODE ISLAND
1998

MASTER OF SCIENCE THESIS

OF

CORRIE MODELL ALJIAN

APPROVED:

Thesis Committee

Major Professor Mark Wimbush

DEAN OF THE GRADUATE SCHOOL

UNIVERSITY OF RHODE ISLAND

1998

Abstract

This thesis analyzes three observational data sets related to the El Niño/Southern Oscillation (ENSO) phenomenon to determine if ENSO can be considered as a low-dimensional chaotic system. In order to test this hypothesis, I apply *Barahona and Poon*'s [1996] method for detecting nonlinear determinism in short, noise-contaminated time series, and calculate the correlation dimension, D_c. A slightly modified version of the *Vallis* [1986] model is used to provide a context for interpreting the results, and to validate the computations done on the observational data.

When applied to observational ENSO data, the Barahona and Poon algorithm indicates that low-order nonlinear mapping functions have predictive power which is not significantly different from linear models. In contrast, when the algorithm is applied to correspondingly sampled data from the Vallis model, the algorithm shows the presence of nonlinear determinism, even when these data are strongly contaminated with noise.

There is a weak convergence of the correlation dimension in the observational data to a D_c value between 8 and 10. This indicates that the phase-space dimension of ENSO is at least 8.

These results suggest that either (1) ENSO is not governed by low-dimensional nonlinear dynamics, or (2) noise related to local physical processes overwhelms the ENSO chaotic signal in the observational data.

Acknowledgment

There are many people whose help was beyond value in putting this thesis together. First among those people, I'd like to thank Dr. Mark Wimbush, my major professor. His idea is what started this project, and his ideas helped to bind it into a cohesive whole.

Also, my gratitude goes to my thesis committee chair, Dr. Robert Costantino and to Dr. Ken Hartt, for explaining the theoretical underpinnings of chaos theory (and the sorting algorithm, developed by Dr. Leonard Kahn at URI, behind my Grassberger-Procaccia calculations) and to my other thesis committee member, Dr. Chris Kincaid, for his helpful comments and enthusiasm.

My thanks to Dr. Chi-Sang Poon for providing the Matlab routines I use to apply the Barahona and Poon algorithm, and for the time he took to explain them to me.

Dr. John Merrill and Ruth Platner obtained the Australian gridded data set from the data support section of the National Center for Atmospheric Research.

John Grinstead, Sam Cleland, and Robin Tihema at the Northern Territory Regional Office of the Australian Bureau of Meteorology provided the Darwin SLP data set.

Andrey Karachintsev gave me LaTex advice and templates.

My ex-officemate, Charles James, provided C++ programming advice, and my current officemate, Jeff Book, listened to my constant complaints about computers.

Finally, I'd like to thank my husband, Brian Matthew Aljian, for being my all purpose "tech-support" guy, and my father, Leslie David Modell, for raising me to believe that women can and should pursue any career – especially science.

Contents

List of Figures

1 Introduction

El Niño/Southern Oscillation (ENSO) is an interannual climatological disturbance centered on the tropical Pacific, and it has global effects and relevance. In this thesis, I investigate the possibility that variability associated with ENSO can be attributed to low-dimensional, dissipative, chaotic dynamics.

1.1 ENSO

The term "Southern Oscillation" describes a fluctuation in the Southern Hemisphere's atmospheric pressure over the tropical Pacific and Indian Oceans [*Philander*, 1990]. When surface pressure is high over the eastern Pacific, it tends to be low over the eastern Indian Ocean and vice versa. The two regions for which this negative correlation is largest are referred to as the "centers of action." "El Niño" refers to an appearance of anomalously warm surface waters off the coasts of Peru and Ecuador. El Niño events, also referred to as ENSO events, are coincident with the Southern Oscillation state being such that the atmospheric pressure is low in the east and high in the west. The time interval between successive ENSO events averages about 4 years, but these intervals range from one to eight years in length. ENSO and the Southern Oscillation are considered to be part of a regional cycle with global effects.

Some studies of observational ENSO time series have suggested the possibility of low-dimensional chaotic determinism in ENSO's dynamics [*Elsner and Tsonis*, 1993; *Bauer and Brown*, 1992; *Hense*, 1987]. Additionally, several ENSO models

exhibit chaotic properties [*Tziperman et al.*, 1995; *Jin et al.*, 1994; *Münnich et al.*, 1991; *Vallis*, 1986, 1988]. The *Vallis* [1986] model is used in this work; it is described in Section 3.

Poor prediction of ENSO events has an important effect on the world economy [*Philander*, 1990]. Conventional models and prediction schemes did not anticipate the recent large ENSO event [*CPC*, 1997]. If ENSO can be shown to behave in a manner consistent with low-dimensional chaos, then it is possible that chaotic prediction techniques can be fruitfully employed to forecast future ENSO events.

1.2 Chaos

Chaos refers to the seemingly erratic time-dependent behavior that can occur in otherwise simple, deterministic systems. To be termed chaotic, a bounded time series must not be asymtotically periodic, and it must have at least one positive Lyapunov exponent.[1] For this work, I focus on low-dimensional dissipative chaos, which is operationally defined as a bounded chaotic system having a dimension significantly less than ten. Nonlinearity is a necessary — but not sufficient — condition for chaotic dynamics.

If ENSO is chaotic as described above, what would that mean? In reality, ENSO is governed by a vast number of equations describing the Newtonian physics which all of the molecules in the atmosphere and the ocean must obey. Even with the

[1] The Lyapunov exponents quantify the exponential divergence (in time) of initially close trajectories. If the vector distance between two nearby trajectories goes as $\vec{s} = \vec{s_0}e^{Lt}$, then the eigenvalues of the matrix L are the Lyapunov exponents for that system.

continuum hypothesis, the effective scale of the smallest fluid motions in the ocean is of order 1 cm, and there are 10^{24} such centimeter-size parcels in the ocean. If ENSO is governed by low-dimensional nonlinear dynamics, only a much smaller number of equations is important in interpreting and predicting the dynamics. Thus, there would exist a simple model capturing all of the important physics of the system. Nevertheless, knowing this would not in itself tell us anything about the feasibility of finding that model, or about the uniqueness of that model.

Two methods were used to examine the degree of nonlinearity in ENSO data sets. Originally, I also planned to calculate the Lyapunov exponents for the ENSO attractor, however, that calculation relies on knowledge of an upper bound for the fractal dimension of the attractor. The results from the two methods cited in this study (Sections 4 and 5) indicate that Lyapunov exponents are essentially incalculable from the available data sets.

The first method used is taken from *Barahona and Poon* [1996]. This method finds appropriate linear and nonlinear iterated map models for the given data set. It then calculates a "goodness of fit" metric for those linear and nonlinear models. If a nonlinear model has significantly greater predictive power than the linear model, then the data set is said to have underlying nonlinear deterministic dynamics. This method is described in greater detail in Section 4.

The second computation done for this work is the calculation of the correlation dimension [*Grassberger and Procaccia*, 1983] for the climate time series. If time series data are taken from all of the phase variables of a chaotic system, they will lie on a chaotic orbit, a "strange attractor." The fractal dimension of this attractor

can be calculated on a subset of those variables (or a linear combination of that subset) to reconstruct an analog to the original phase space. The theory of time-delay embedding says that even a single time series can be used in this manner, and the correlation dimension of the reconstructed orbit constitutes a lower bound for the actual number of independent variables controlling the time evolution of that system. For high enough embedding dimensions, the correlation integrals should be approximately linear in log-log space. The slope of that line is the correlation dimension. The details of this method are described in Section 5.

Section 6 summarizes the results and concludes the main part of this thesis.

2 The Data Sets

2.1 SOI

The Southern Oscillation Index (SOI) is a standardized, monthly-averaged sea-level atmospheric pressure (SLP) difference between Tahiti and Darwin, Australia. Strongly negative SOI values are associated with ENSO events. Tahiti and Darwin are chosen because they are near the centers of action for the Southern Oscillation [*Philander*, 1990] and because there is a large enough quantity of high-qualitiy data available to make a consistent time series. The version of the SOI used in this study is the Climate Prediction Center (CPC) standardized SOI. The data set starts September, 1932 and it continues through April, 1998. The CPC archives the SOI from 1880 through the present, but there are several large data gaps during 1880–1932, so the set used here starts at the end of the last such gap. Thus, 788 monthly-averaged data points were used for this study. This data set is referred to as the "SOI". For more details, see Appendix A.

2.2 Daily T-D

The short length of the SOI limits the accuracy of the computational procedures used in this study. However, lengthy historical measurements are hard to come by, and in any event would not extend significantly farther back into the past than the SOI does. The only other option, then, is to obtain data with a higher time sampling rate than the SOI's monthly rate. To address this need, a daily analog to the SOI was computed for these analyses from a spatially gridded data set.

Although I obtained the base data set through tape archives [*Walters*, 1997] at the National Center for Atmospheric Research, it was originally produced at the Australian National Meteorological Research Centre [*Seaman, et. al.*, 1995]. It employs time and spatial averaging to fit all available SLP data (from 4/24/1972 through 12/31/1992) to a 47×47 grid extending across the southern Pacific region. It lists SLP values daily for the grid points at Greenwich Mean Time (GMT) 23:00 until 4/8/73, and twice a day at 11:00 and 23:00 GMT thereafter.

The spatial bins used for this set are about 350 km across (at 17°S). Because the size of the area represented by a grid point is so large, only one grid point was used to acquire the SLP at Tahiti and one at Darwin. The grid points used are: (9,33) centered at 16.4472°S, 149.036°W for Tahiti, and (12,10) centered at 13.5319°S, 130.601°E for Darwin.

After extracting the appropriate data from the archive, a daily composite data set was calculated. For days with two available data points, an average of the two points was used. For days with only one data point available, that point was used. There were 69 missing days with no individual gap being more than 9 days long, so a cubic spline interpolation was calculated to fill in for those days with zero available data points. Finally, the daily SLP value for Darwin was subtracted from that for Tahiti. Altogether, 7557 such "pseudo-SOI" values were computed. These data will be referred to as the "T-D" (Tahiti minus Darwin) data set.

2.3 Darwin SLP

To compliment the other two data sets, a daily SLP time series at Darwin was constructed. The Darwin data set is used separately because it is a directly measured data set, and because it has the largest number of available daily data points (16895). However, the Darwin SLP series has a large seasonal component, which could interfere with the calculation of ENSO statistical and chaotic properties.

Eight-times-daily SLP data for Darwin were obtained directly from the Australian Bureau of Meteorology. This data set spans the time period from July 1, 1951, 2:00 local time, through September 30, 1997, 21:00 local time. To reduce the impact of the diurnal cycle, a daily average was taken by directly averaging all of the available data points between 0:00Z and 23:59Z. Except for one day, every day had at least 3 measurements. That one day had no data, and the SLP for that one day was taken to be the average of the SLP measurements for the previous and following days. Finally, 1000 mbar was subtracted from each SLP value. This processing resulted in a (residual) SLP series 16895 days long. The data set will be referred to as the "Darwin SLP" data.

2.4 Random numbers

For the analysis techniques used in this work, it is helpful to compare the results with an equivalent random data set. Therefore, for each data set, a surrogate data set was constructed following the method described in *Tsonis and Elsner* [1993]. The Fourier transform of the data set was computed, and then the frequency amplitudes

were multiplied by a random phase factor, $e^{i\phi}$, where ϕ is uniformly distributed in the interval 0 to 2π. The inverse transform was then used as a surrogate series. This process produces a random series with a mean, variance, and autocorrelation function similar to the original series. Although in theory the inverse transform of the newly randomized data should be real if $\phi(f) = \phi(-f)$, in practice, numerical errors induced a significant imaginary part to the inverse. Thus, for this analysis two additional computational steps were performed. First, the imaginary part of the inverse transform was dropped (the real part was used). Secondly, the standard deviation, σ, was manually adjusted to match the σ of the original time series. Inspection of the random time series obtained in this way indicated that their autocorrelation functions match those of the original data sets well. Figure 1 shows the autocorrelation functions for the SOI and its corresponding random surrogate data set.

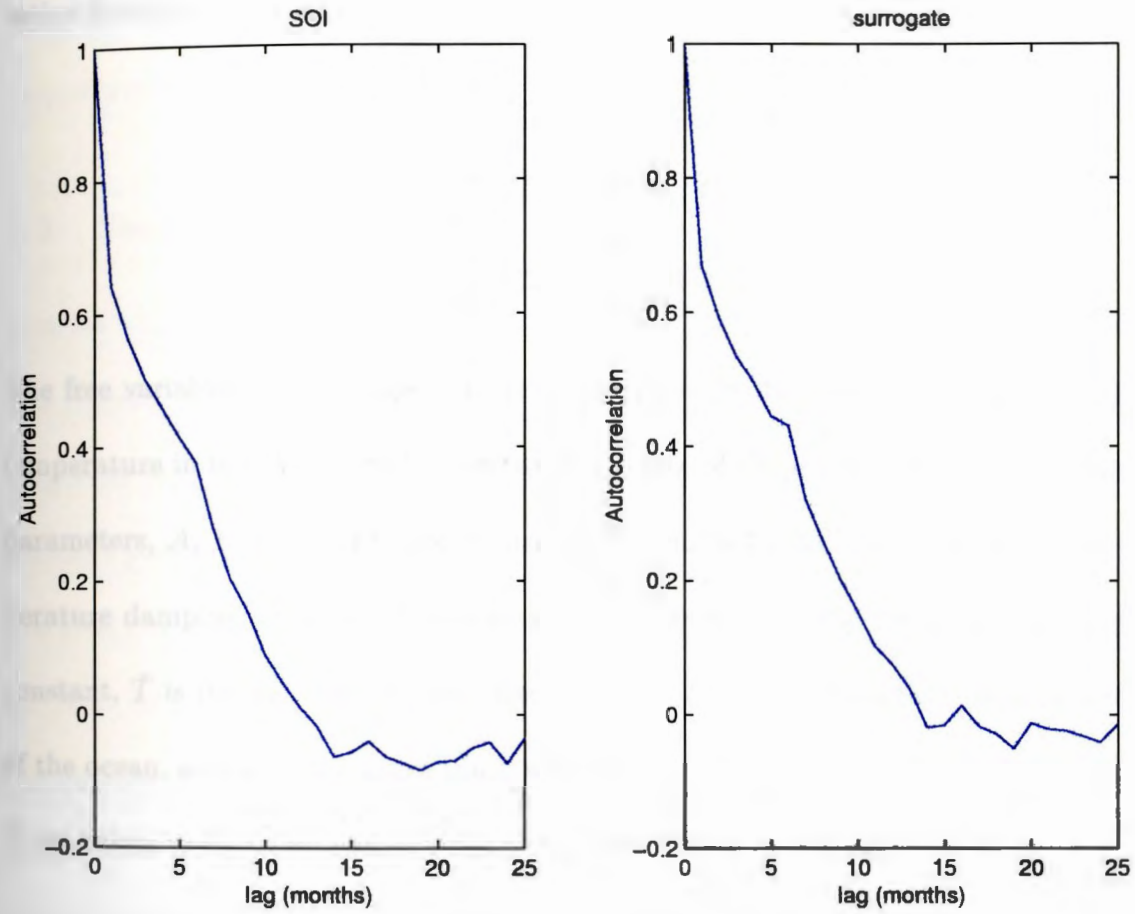

Figure 1: Autocorrelation functions for the SOI (left) and its random surrogate (right).

3 The *Vallis* Model

3.1 Model Physics

Vallis [1986] proposed a simple model for ENSO which captures many of its qualitative features. The Vallis equations are

$$\begin{aligned}
\frac{du}{dt} &= \frac{B}{2\Delta x}(T_e - T_w) - C(u - u^*) \\
\frac{dT_w}{dt} &= \frac{u}{2\Delta x}(\bar{T} - T_e) - A(T_w - T^*) \\
\frac{dT_e}{dt} &= \frac{u}{2\Delta x}(T_w - \bar{T}) - A(T_e - T^*).
\end{aligned}$$

The free variables are T_e (upper-ocean temperature in the East), T_w (upper-ocean temperature in the West), and u (eastward velocity of the upper-ocean). The other parameters, A, B, C, $\bar{T}$, T^*, and u^* are predetermined. A is the Newtonian temperature damping constant, B is a coupling constant, C is the frictional damping constant, $\bar{T}$ is the mean deep-ocean temperature, T^* is the relaxation temperature of the ocean, and u^* is the mean trade wind velocity. In this research, A, B, C, and $\bar{T}$ are taken to be the values suggested by *Vallis* [1986] (see table below)

parameter	value
A	0.083333 month^{-1}
B	2 m^2 sec^{-2} °C^{-1}
C	0.25 month^{-1}
$\bar{T}$	0 °C

which are chosen to correspond to the real ocean dynamics, and to make one time unit correspond to about one month, but T^* and u^* are adjusted to match the observed ENSO dynamics more closely. Figure 2 shows 2000 months of *Vallis* model data. This figure, as with all Vallis model data sets used in this thesis, was calculated using a fourth-order Runge-Kutta integration with $\delta t = 0.05$ month. The model output with this time interval is refered to as the Vallis "daily" data set.

3.2 Seasonal Forcing

Because the tropical Pacific Ocean is strongly influenced by seasonal forcing, for this research a seasonal forcing is included. In his original paper, *Vallis* [1986] suggested that a seasonal forcing could be added to the model by replacing the constant parameter, u^*, with $u^*(t) = \mathrm{u}^*(1 + 3\sin\omega t)$, where $\omega = \frac{2\pi}{1\mathrm{year}}$. However, this level of seasonal variation implies that the trade winds reverse for almost half of the year. According to *Philander* [1990], the real trade winds only reverse for about two months in the spring. In order to make the seasonal forcing more realistic, this research uses $u^*(t) = \mathrm{u}^*(1 + \alpha\sin\omega t)$ and α is a constant amplitude chosen to make the trade wind reversal occur for only two months in the spring (see Figure 3). Using Vallis's value $\mathrm{u}^* = -0.45\,\mathrm{ms}^{-1}$ and taking $t = 0$ to be the beginning of the year, this requires that $\alpha = -1.1$.

3.3 An analog to the SOI

Both the computational methods used here assume that only one time series is available, but the Vallis model has three independent phase variables. To make comparisons between the model and the data, one needs to choose which of the phase variables to use as a proxy to the data. I decided to use the phase variable which showed the clearest difference between the model "ENSO" and "normal" states. Figure 4 shows histogram plots of the variable values when they were at relative maxima. These were calculated for T^* values which ranged from 2° to 20°C (with a step size of .01°C). At each T^* value, the model was iterated to produce 120,000 months of data and all of the model runs were combined to produce Figure 4. There are two distinct groups in the histogram for u corresponding to the ENSO and non-ENSO conditions. Hence, it is easy to define an ENSO criterion in terms of the relative maximum of u. I have chosen the relative maxima of u being greater than 1 to be my criterion for defining an ENSO condition, but any value between .9825 and 1.825 would have given identical results.

3.4 Justification for T^* change

In order to make the frequency of ENSO event occurrences in the model match that of the SOI, the model T^* parameter was adjusted.

First, the SOI ENSO event rate was calculated as follows. The SOI data set was smoothed using a 12-month-period low-pass Butterworth filter (applied in both the forward and reverse directions). Then as with Figure 4, a histogram of the relative

SOI minima was plotted (see Figure 5) to find a suitable threshold SOI value for determining ENSO events. The pronounced minimum at SOI = -0.9 suggests this as an appropriate threshold value. Finally, the number of SOI relative minima below this threshold were considered to be ENSO events (with a threshold value of -0.9, there were 15 ENSO events), and the ENSO rate was calculated by dividing the number of SOI relative minima by the total number of years in the data set (788 months = 65.67 years). This resulted in an SOI ENSO rate of 0.2284 year^{-1}.

Second, the model ENSO rate was calculated as a function of T^*. This is shown in Figure 6. Again, a model ENSO event occurs (by definition) when a relative maximum of u is greater than 1. The number of relative maxima which were ENSO events is divided by the total number of years (12 model months) to calculate the model ENSO rate for each T^* parameter value between 2° and 20°C in increments of 0.01°C. The model ENSO rate matches that of the SOI when T^* is 7.32°C.

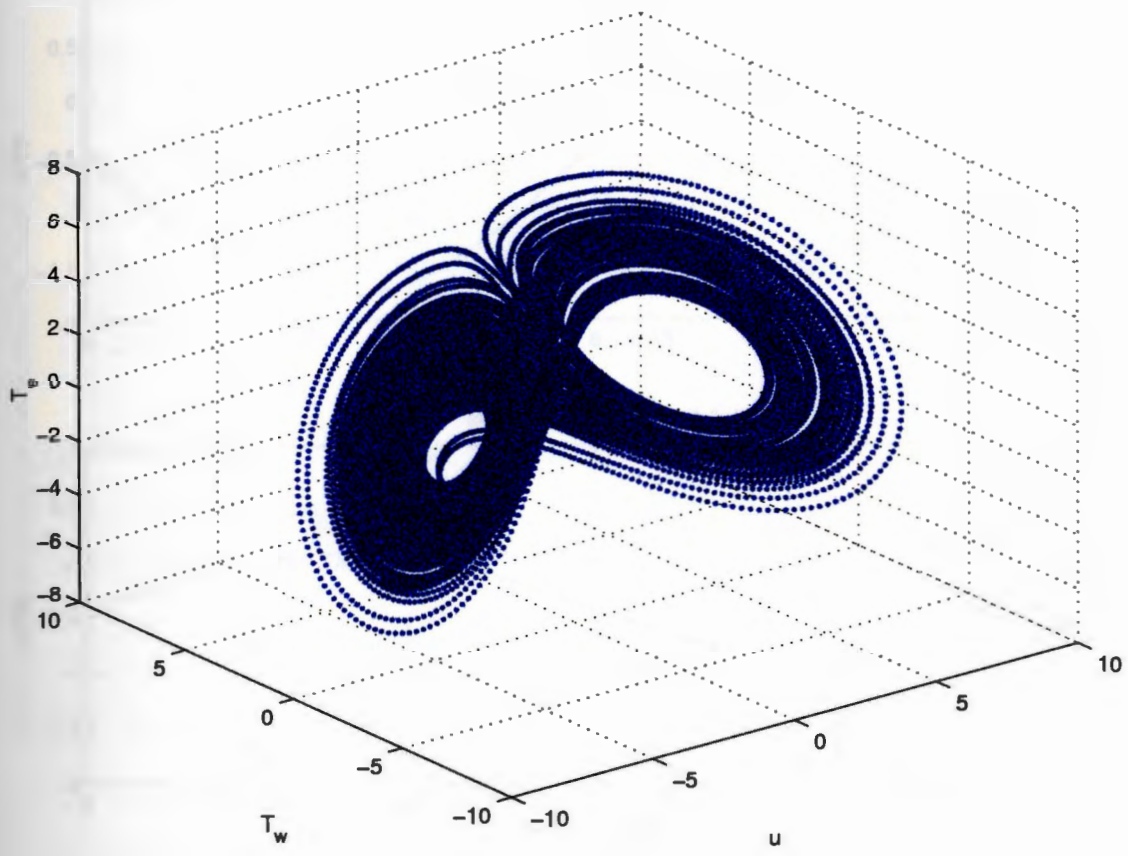

Figure 2: 2000 months of periodically forced Vallis model u, T_e, and T_w data with $\alpha = -1.1$, and $T^* = 7.32°C$ (see Sections 3.2 and 3.4.) Note that the system orbits two attraction zones corresponding to positive and negative u values. When the relative maximum of $u > 1$, a model "ENSO" event is said to have occurred. Also note that there are fewer orbits around the $u > 1$ side of the attractor.

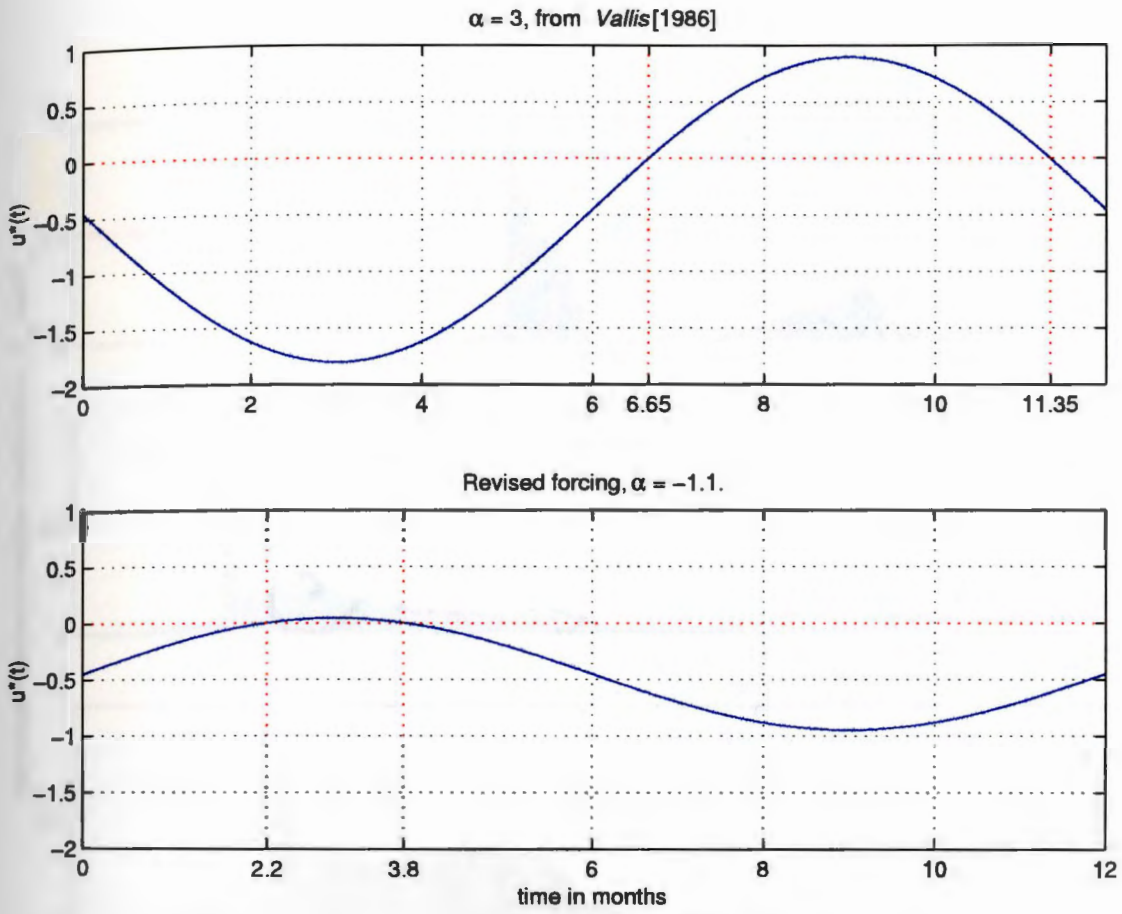

Figure 3: Seasonal Forcing functions, $u^*(t) = \mathrm{u}^*(1+\alpha \sin \omega t)$, $\mathrm{u}^* = -0.45\,\mathrm{ms}^{-1}$, and $\omega = 2\pi/1\mathrm{year}$.

Top: Original seasonal forcing function, as suggested by *Vallis* [1986], here $\alpha = 3$.

Bottom: The revised forcing function used for this research, where $\alpha = -1.1$. Note that the trade winds reverse ***slightly*** in mid-March through mid-April (months 2.2 through 3.8).

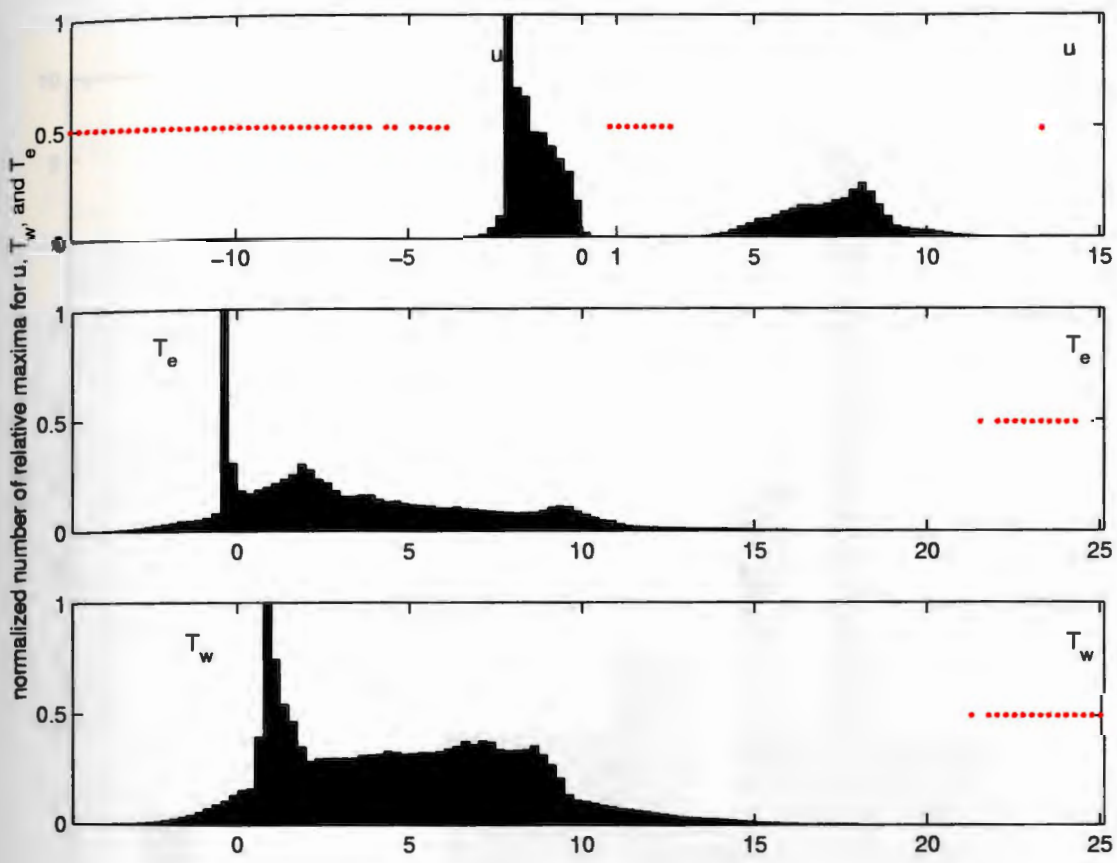

Figure 4: Histograms of relative maxima for Vallis model variables with bin widths 0.25 units, calculated for T^* between 2°C and 20°C (see text). The number of relative maxima has been normalized so that the highest number in each plot is exactly one. The red dots mark the bins which have zero points in them.

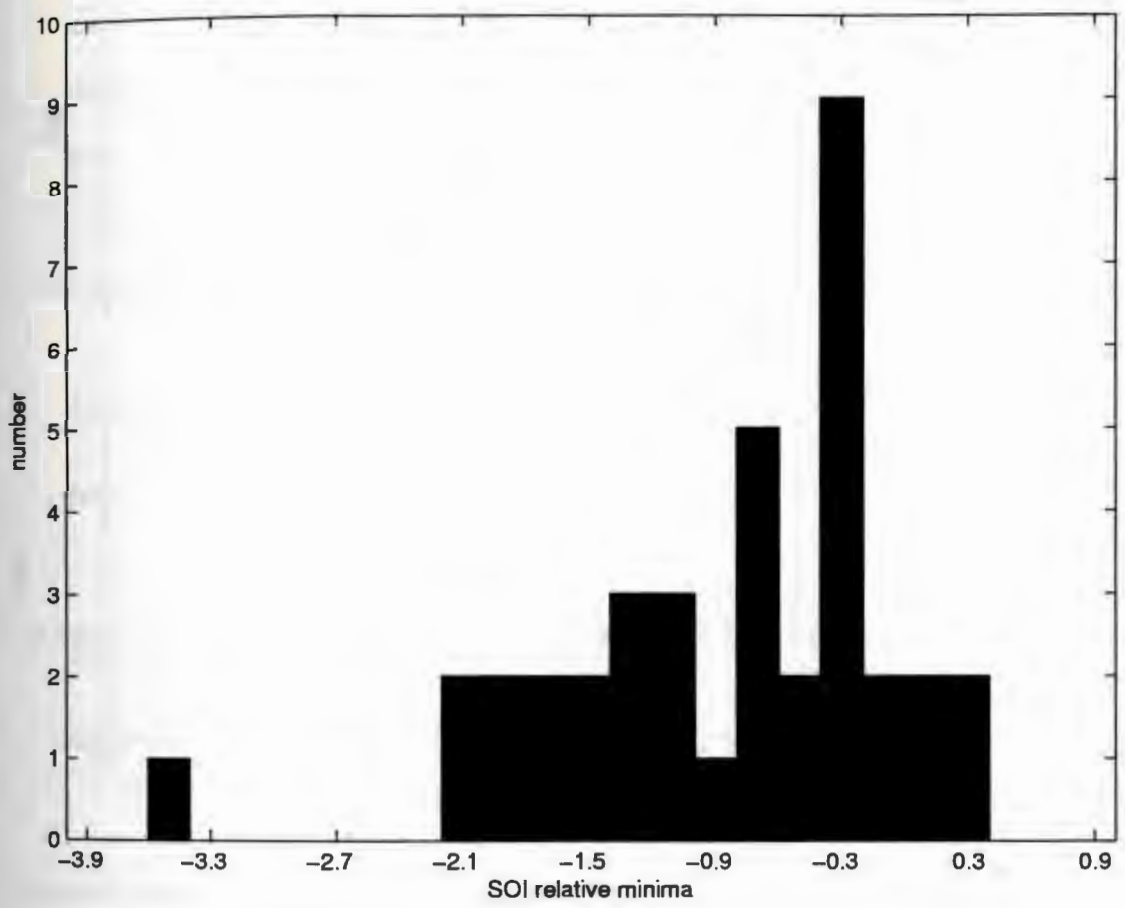

Figure 5: Histogram of relative minima for the SOI data set with bin width 0.2 units.

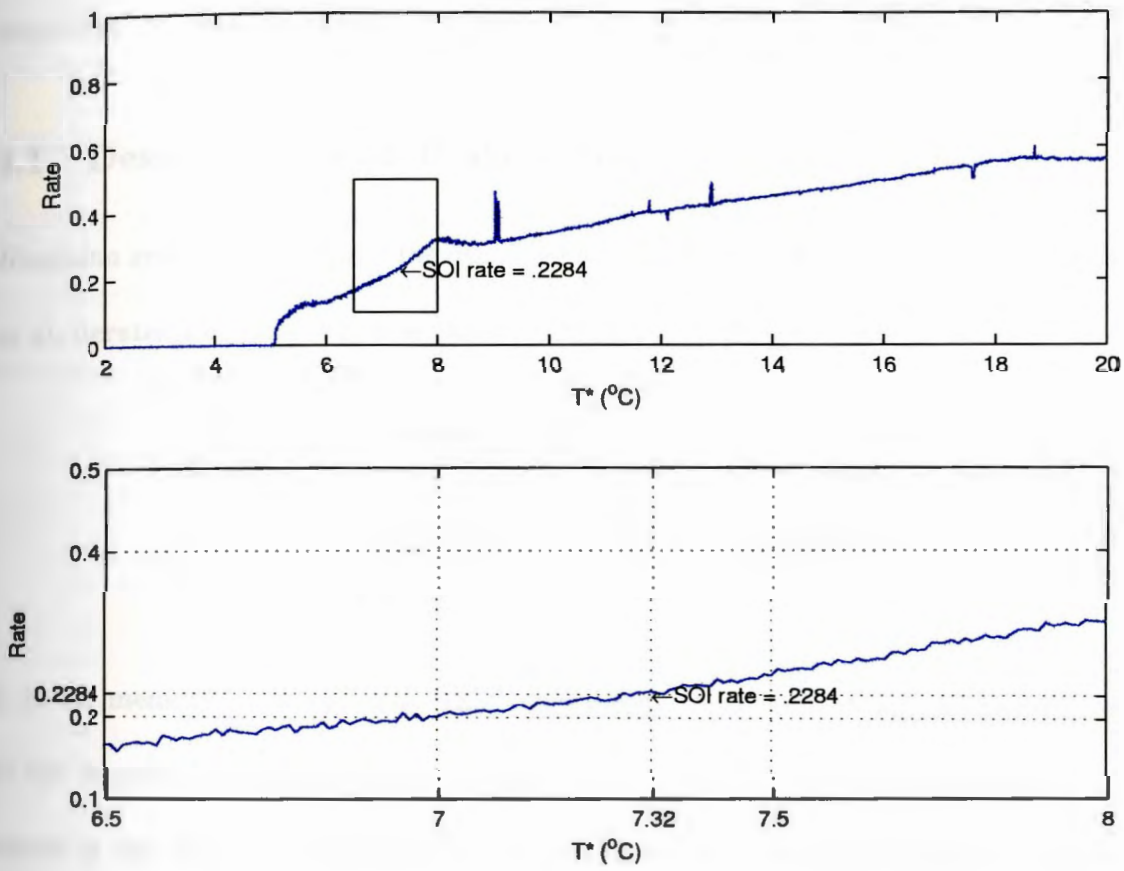

Figure 6: ENSO rates for the periodically forced Vallis model as a function of T^*. In the top panel, the ENSO rate calculated from the observed SOI is marked. The bottom is an enlargement of the section delineated in the top panel. The point (7.32,0.2284) defines the T^* value used for the Vallis model runs.

4 B/P analysis

Barahona and Poon [1996], describe a method for detecting nonlinear determinism in short, noisy time series. That algorithm is used here and referred to as the "B/P algorithm" or "B/P analysis".

4.1 Description of B/P algorithm

Barahona and Poon [1996] use the discrete Volterra-Weiner-Korenberg (VWK) series as an iterated mapping function, where $y_n = y_n(y_{n-1}, y_{n-2}, \ldots, y_{n-\kappa})$. So,

$$\begin{aligned} y_n^{calc} &= a_0 + a_1 y_{n-1} + a_2 y_{n-2} + \cdots \\ &\quad + a_\kappa y_{n-\kappa} + a_{\kappa+1} y_{n-1}^2 + a_{\kappa+2} y_{n-1} y_{n-2} + \cdots \\ &\quad + a_{M-1} y_{n-\kappa}^d \,. \end{aligned} \tag{1}$$

κ is the memory of the system (this corresponds to an embedding dimension), d is the degree of the polynomial, and $M = (\kappa + d)!/(d!\kappa!)$ is the total number of terms in the complete expansion. The coefficients, a_m, are then calculated to find a best-fit VWK mapping function to the data. The parameters κ and d are chosen to minimize Akaike's information criterion,

$$C(r) = \log \varepsilon(r) + r/N, \tag{2}$$

where $r \leq M$ is the number of mapping function terms used to make short-term predictions on the data, and ε is the standard one-step-ahead prediction error of those predictions. $C(r)$ essentially measures the "goodness of fit" of the mapping function to the data, where a low $C(r)$ value means there is a good fit between

the VWK mapping function and the original data. Nonlinear mapping functions are constructed by setting $d \geq 2$, and for comparison, linear mapping functions are constructed by setting $d = 1$ and letting κ vary between 1 and M, where M is the number of terms in the associated nonlinear mapping function. For instance, if $\kappa = 2$ and $d = 2$, then the nonlinear $C(r)$ calculation is calculated for the best-fit VWK mapping functions with $\breve{\kappa} \leq \kappa$, $\breve{d} \leq d$ and $(\breve{\kappa}, \breve{d}) = (1,1), \ldots, (2,2)$, in a recursive fashion. In other words, once a_i is calculated for a given r, that value of a_i is reused for all subsequent r. Figure 7 shows this case for Vallis model u data, and the following table explains what each point on the plot represents.

r	VWK mapping function	$(\breve{\kappa}, \breve{d})$
1	a_0	0 by definition
2	$a_0 + a_1 y_{n-1}$	$(1,1)$ – complete
3	$a_0 + a_1 y_{n-1} + a_2 y_{n-2}$	$(2,1)$ – complete
4	$a_0 + a_1 y_{n-1} + a_2 y_{n-2} + a_3 y_{n-1}^2$	$(2,2)$ – truncated
5	$a_0 + a_1 y_{n-1} + a_2 y_{n-2} + a_3 y_{n-1}^2 + a_3 y_{n-1} y_{n-2}$	$(2,2)$ – truncated
6	$a_0 + a_1 y_{n-1} + a_2 y_{n-2} + a_3 y_{n-1}^2 + a_3 y_{n-1} y_{n-2} + a_3 y_{n-2}^2$	$(2,2)$ – complete

$C(r)$ is calculated for nonlinear and linear VWK mapping functions of the original data, and both such mapping functions are compared to the $C(r)$ function for a linear mapping function of a random surrogate to that data set. (The surrogate data set is always recalculated from the given data set.) If $C(r)$ for the nonlinear mapping function is significantly lower than that of the linear mapping function and the surrogate data, then the data set displays nonlinear deterministic dynamics. In

Figure 7 note that the nonlinear $C(r)$ function is *not* smaller than those of the linear and surrogate-linear VWK mapping functions. The data set is chaotic, so in principle, the algorithm should pick up nonlinear determinism. It does not, because $\kappa = 2$ (the embedding dimension) is smaller than the actual model phase space dimension of 3. Figure 8 shows the results for B/P analysis of the same data set with $\kappa = 5$, $d = 4$. Here the nonlinear $C(r)$ function lies well below the linear and surrogate $C(r)$ functions for $r > 21$, indicating nonlinear determinism as expected.

Also, in practice, the number of terms, M, in the VWK expansion should be much less than the length of the time series. Thus, there are limits on the magnitudes of κ and d, and when the time series are short, this method is only useful in characterizing low-dimensional nonlinear dynamics.

4.2 SOI

Figure 9 shows the B/P algorithm applied to the SOI data set. The parameter values of $\kappa = 7$ and $d = 3$ ($M = 120$) were chosen to maximize κ without making the maximum number of terms in the VWK series too long compared to the length of the data set. (Other values of κ and d, with $M < 130$ were tried with similar results.) As is apparent from Figure 9, the linear and nonlinear mapping functions, and the mapping function based on a random surrogate to the SOI, have similar predictive capabilities. This indicates that ENSO is not driven by a nonlinear, deterministic dynamical system with a small number of degrees of freedom, or that small-scale phenomena (random noise) overwhelm ENSO, or that monthly averaging of the

climate data (from compiling the SOI) obscures the results. To help distinguish between these possible explanations I use the algorithm on Vallis model data.

4.3 Vallis Model

The Vallis model (as described in Section 3) was used to generate a monthly-sampled data set. The length of the data set is chosen to correspond to the length of the SOI series. To investigate the effects of noise and other potential data problems on the detection of nonlinear determinism in the Vallis model, I set $\kappa = 5$, $d = 4$ (and thus $M = 126$) in applying B/P analysis to this data set. Although other parameter values were tried, the nonlinear character of the data set is the most clear with these parameter values (Figure 8).

4.4 Monthly averaging

Figure 10 shows $C(r)$ functions based on 788 monthly-averaged Vallis model data points. These look nearly identical to those for the monthly sampled output (Figure 8); the monthly averaging did not affect the algorithm's capability.

4.5 Noise

Surrogate noise with standard deviations, σ, up to 100% of the signal standard deviation was added to the model data before the B/P algorithm was applied (Figure 11). When the noise strength was 60% or lower, then the system still displayed identifiable nonlinear determinism. The surrogate $C(r)$ functions in these plots are

surrogates of the noisy Vallis model data. Adding the noise to the Vallis daily data set *before* forming monthly averages produced essentially the same results. So, if the proposed ENSO climate attractor is similar in essence to the Vallis model, the fact that nonlinear determinism was not detected in the observational data puts a lower limit of 60% on the noise level in the SOI data set. In other words, either the SOI is not characterized by low-dimensional nonlinear dynamics, or the noise in the data set is greater than 60%.

4.6 Smoothing

The monthly-sampled Vallis model data set described above with and without added noise (σ = 100% of the signal σ) was smoothed with a low-pass Butterworth filter (run forwards and backwards) before applying the B/P algorithm. The B/P analysis failed to detect nonlinearity for all possible period cutoffs greater than the Nyquist period (2 months), thus smoothing cannot be reliably used to recover nonlinear determinism. This was observed in both smoothed pure data sets (Figure 12) and in smoothed noisy data sets (Figure 13). One possible explanation for this is that a smoothing algorithm increases interdependence among neighboring data points, and this interdependence is linear in nature. Thus smoothing enhances the predictive capabilities of linear mapping functions.

4.7 Sub-sampled Vallis model

A Vallis model data set was constructed to correspond in sampling interval and length with the T-D data set subsampled to 1 data point per 7 days. The data set was subsampled because the B/P algorithm does not work well with oversampled data. By trying various sampling intervals, I found that 1 point per 7 "days" seemed to be the optimal interval in resolving the nonlinear determinism of the Vallis model data when limited to 7557 daily points. 1079 such data points were analyzed (Figure 14).

4.8 Sub-sampled T-D

The B/P algorithm was applied to a data set consisting of 1079 points from the T-D data subsampled to 1 data point per 7 days. The $C(r)$ function for nonlinear mapping functions was not significantly different than the $C(r)$ function for the linear mapping functions or for mapping functions predicting the surrogate data set of the weekly sampled T-D (Figure 15). Thus, the T-D data set is either not characterized by low-order nonlinearity, or there is large localized noise obscuring the low-order nonlinear signal. For this data set, small-scale physical processes have been averaged out by the spatial binning process, so dynamical noise attributed to localized non-ENSO dynamics is not a likely explanation for the null result. Unless the binning process itself destroys the nonlinear signal, this indicates that the Southern Oscillation is a physical system with many significant variables, which this analysis cannot distinguish from "random."

4.9 Bi-weekly-subsampled Darwin SLP

The daily-averaged SLP values from Darwin, Australia were subsampled on a bi-weekly time scale. The resultant time series has 1207 points, and the parameter values used here were $\kappa = 7$, and $d = 3$. The B/P analysis was then applied, and the $C(r)$ for the linear (and surrogate data) mapping functions were smaller than the $C(r)$ for the nonlinear mapping function (Figure 16). Thus nonlinear determinism is not found in this data set.

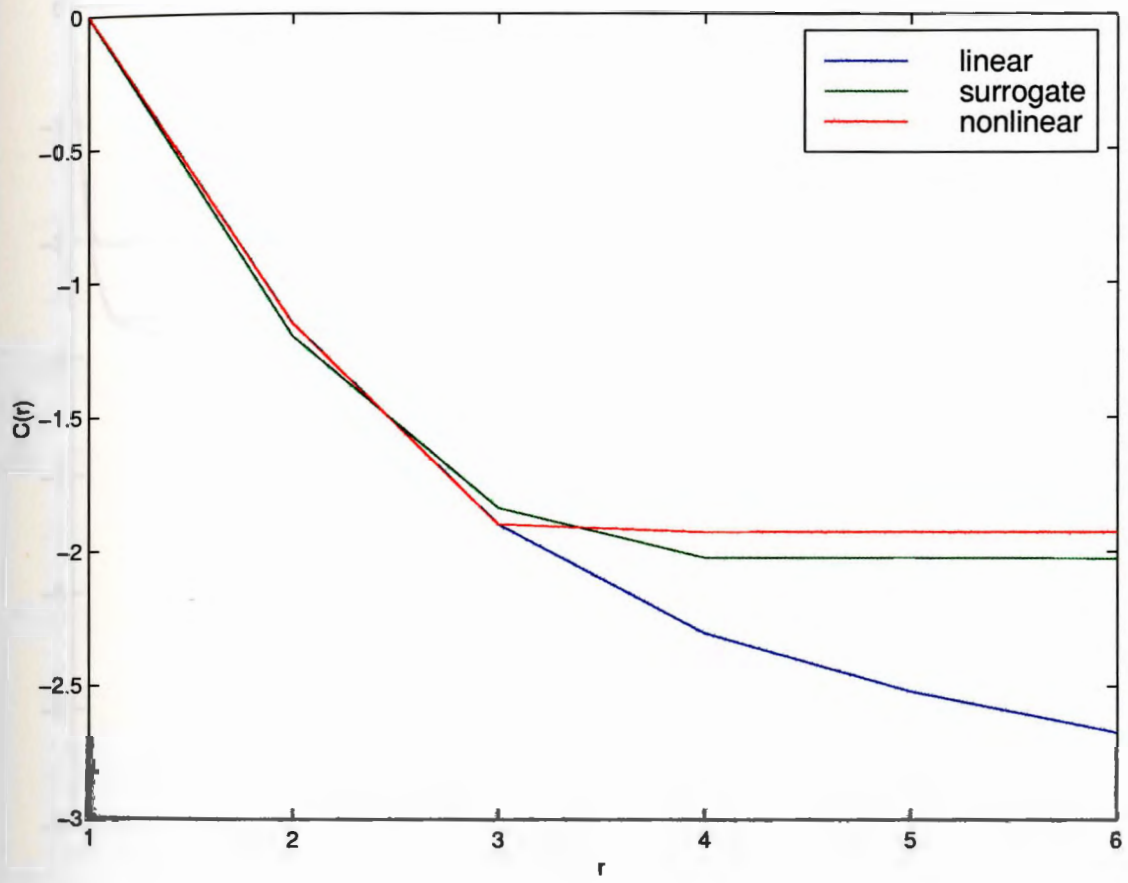

Figure 7: $C(r)$ plot for linear, surrogate-linear, and nonlinear mapping functions with $\kappa = 2$ and $d = 2$ for the Vallis model with 788 points of monthly-sampled u values.

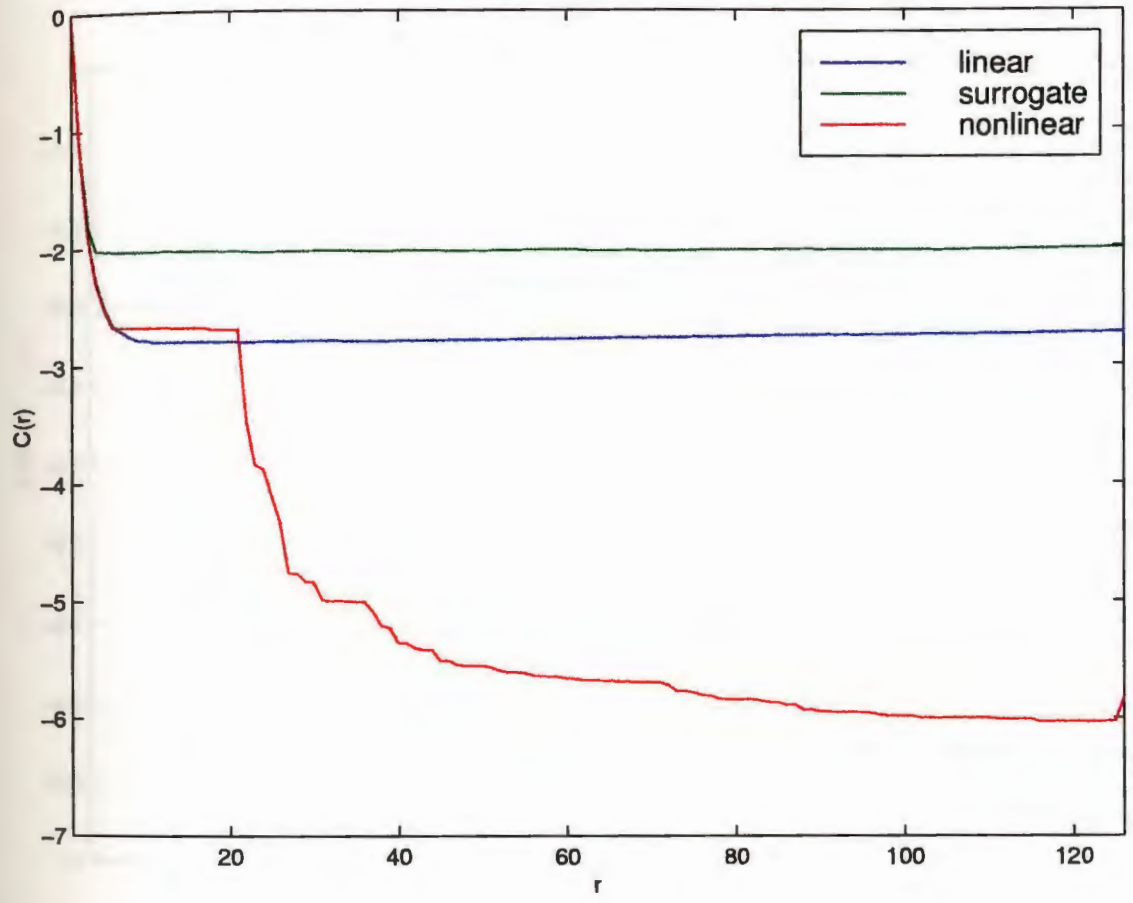

Figure 8: $C(r)$ plot for linear, surrogate-linear, and nonlinear mapping functions with $\kappa = 5$ and $d = 4$ for the Vallis model with 788 points of monthly-sampled u values.

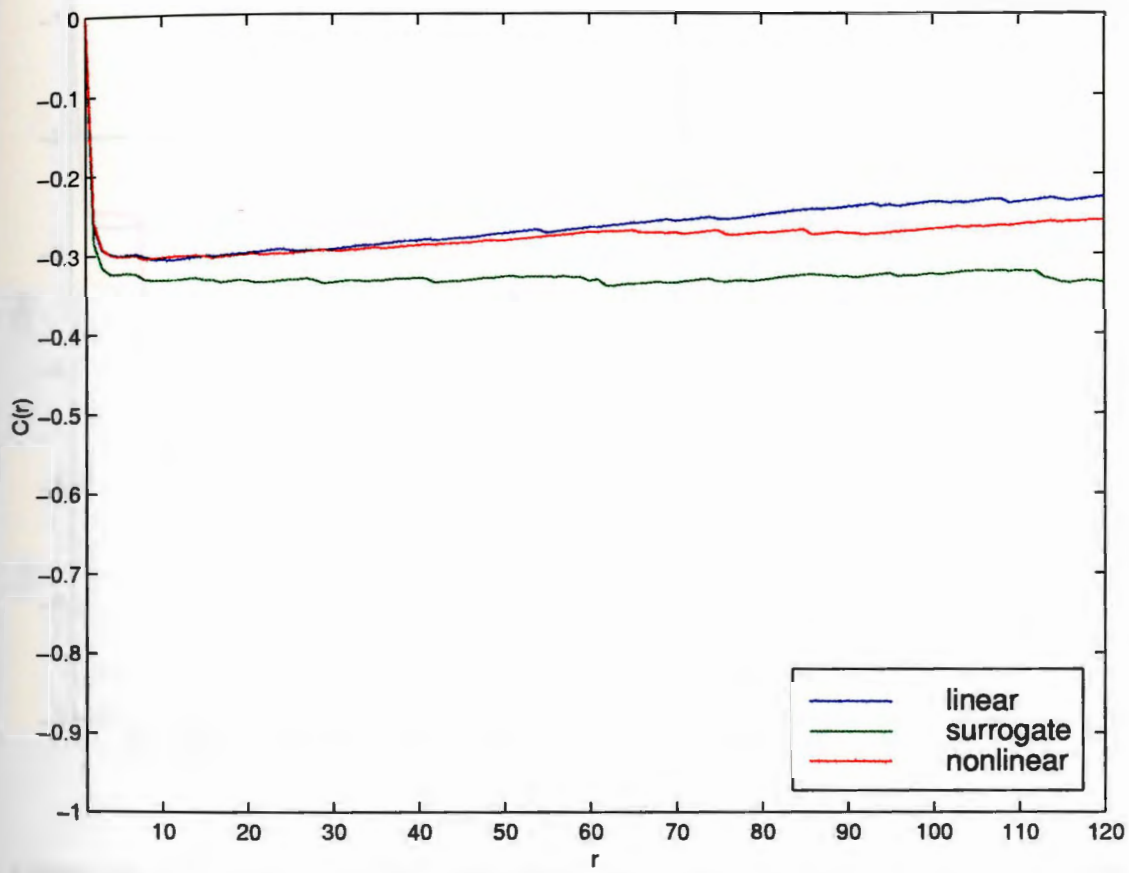

Figure 9: $C(r)$ plots for linear, surrogate-linear, and nonlinear mapping functions with $\kappa = 7$ and $d = 3$ for the SOI data.

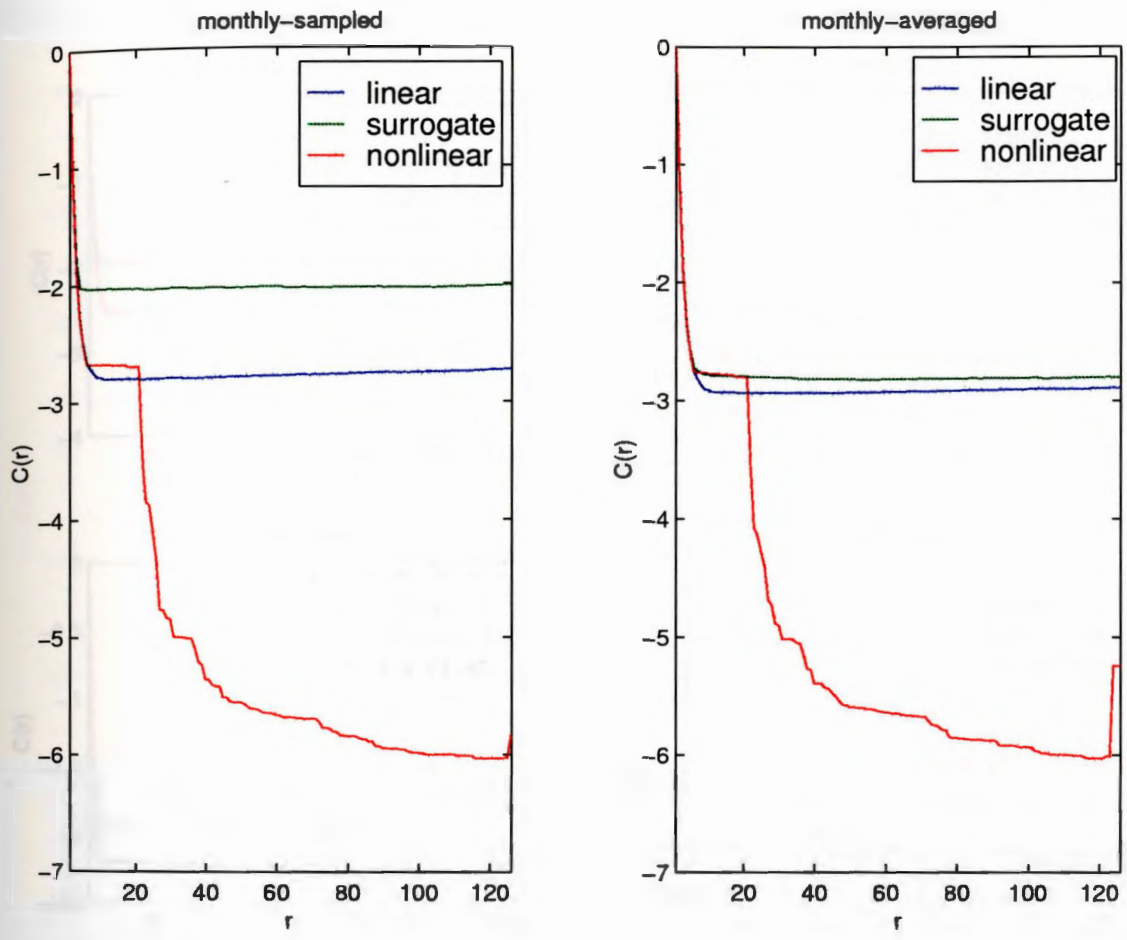

Figure 10: $C(r)$ plots for linear, surrogate-linear, and nonlinear mapping functions with $\kappa = 5$ and $d = 4$ for the Vallis model.

Left: 788 points of monthly-sampled Vallis model u data.

Right: 788 points of monthly-averaged Vallis model u data. The monthly averages were computed from a data set sampled 20 times per month.

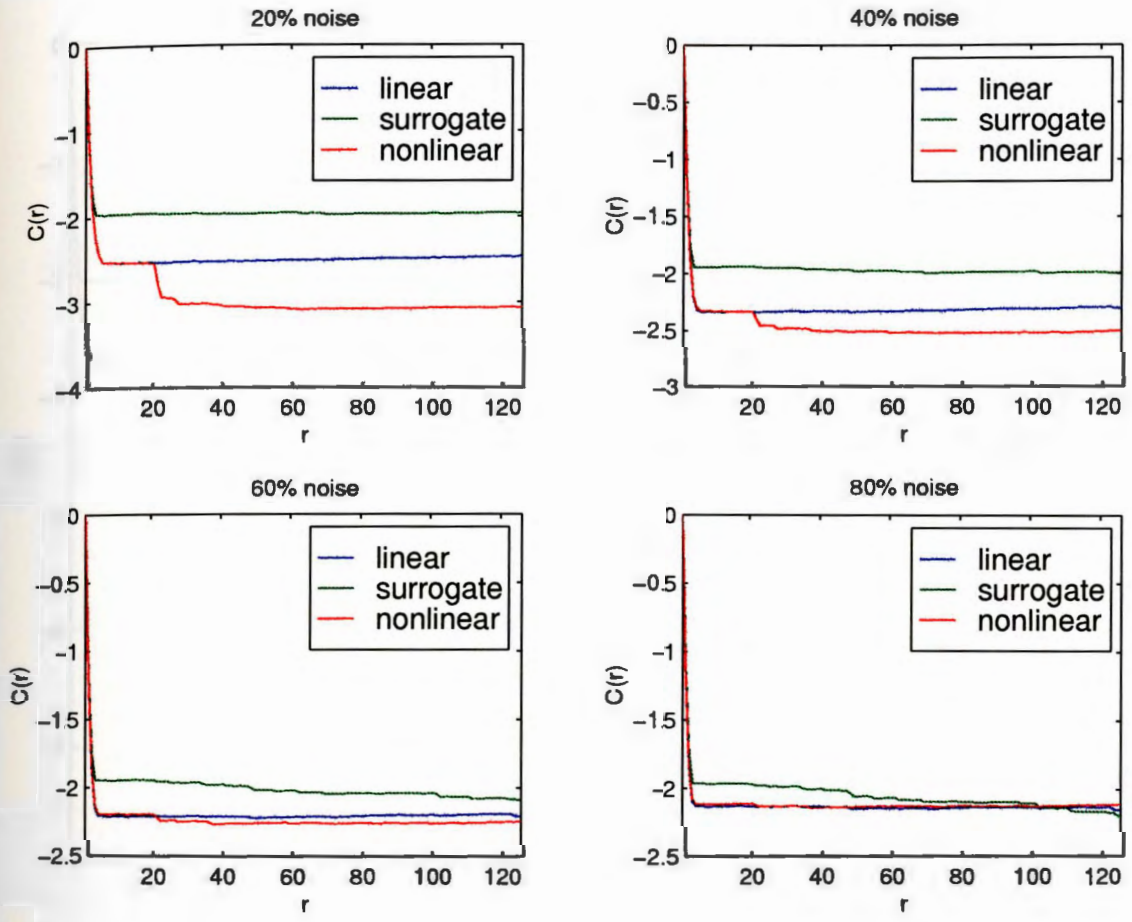

Figure 11: $C(r)$ plots for linear, surrogate-linear, and nonlinear mapping functions for the Vallis model with varying levels of correlated noise. For all panels, $\kappa = 5$ and $d = 4$. (The base data set used here is the same as that used in Figure 8, 788 points of monthly sampled u data).

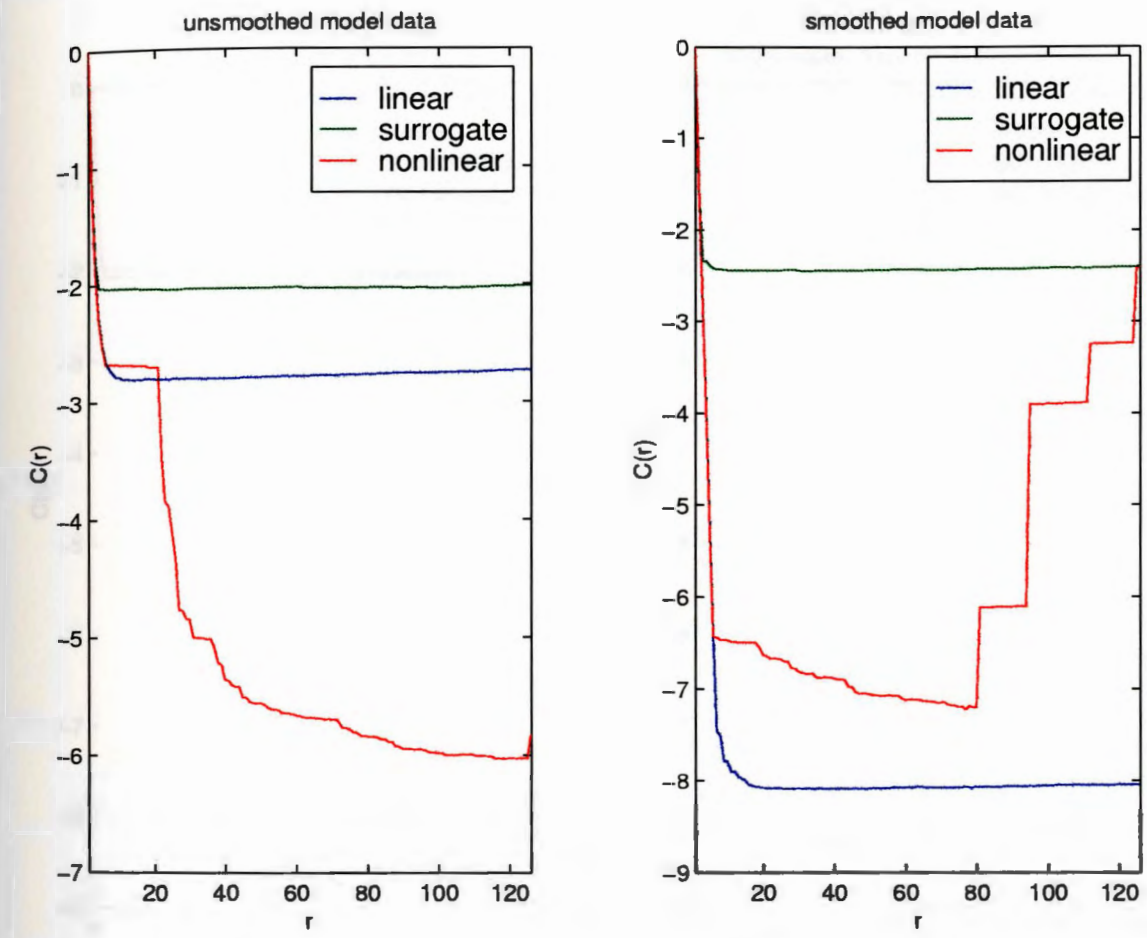

Figure 12: $C(r)$ plots for linear, surrogate-linear, and nonlinear mapping functions for unsmoothed and smoothed (3-month lowpassed) Vallis model data (see text) with $\kappa = 5$ and $d = 4$. One can see that the smoothing alone makes the nonlinearity undetectable with this algorithm.

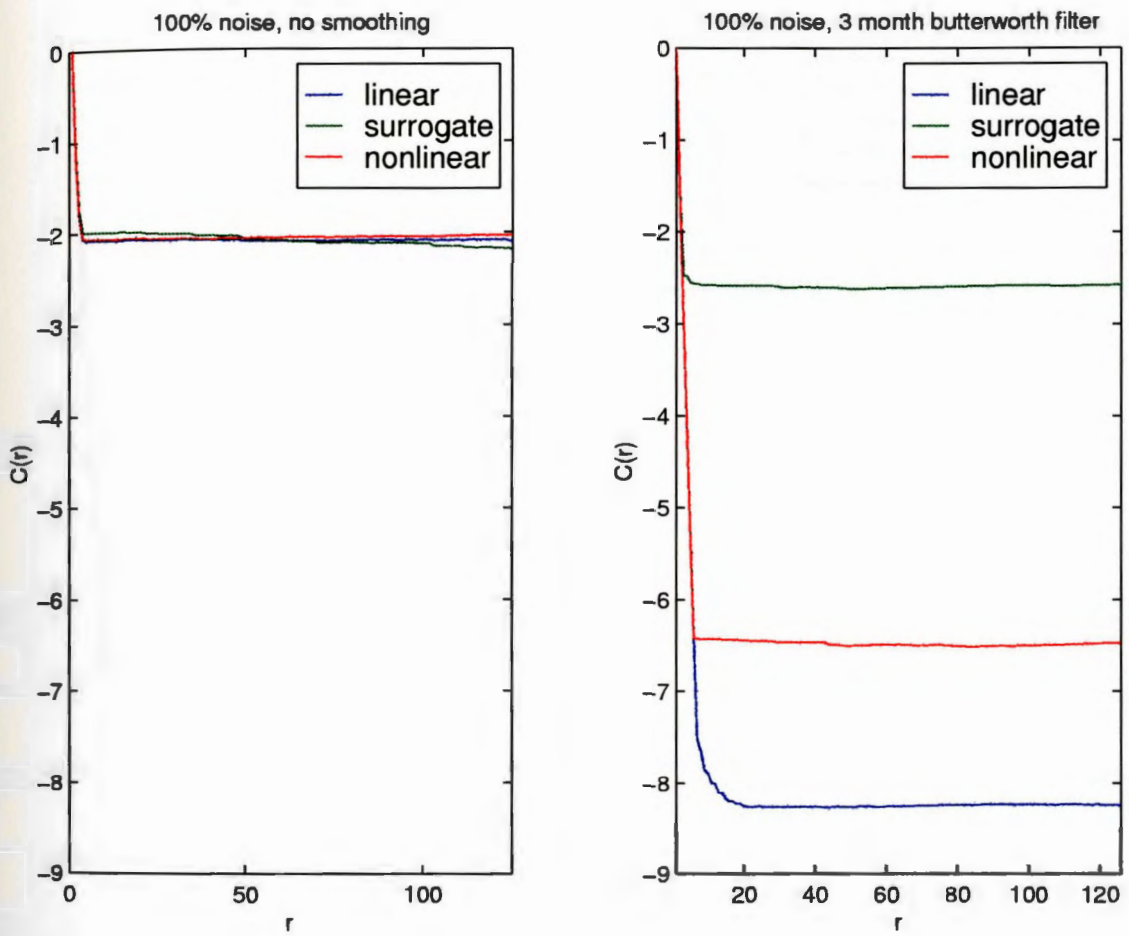

Figure 13: $C(r)$ plots for linear, surrogate-linear, and nonlinear mapping functions for unsmoothed and smoothed (3-month lowpassed) noisy Vallis model data (see text) with $\kappa = 5$ and $d = 4$.

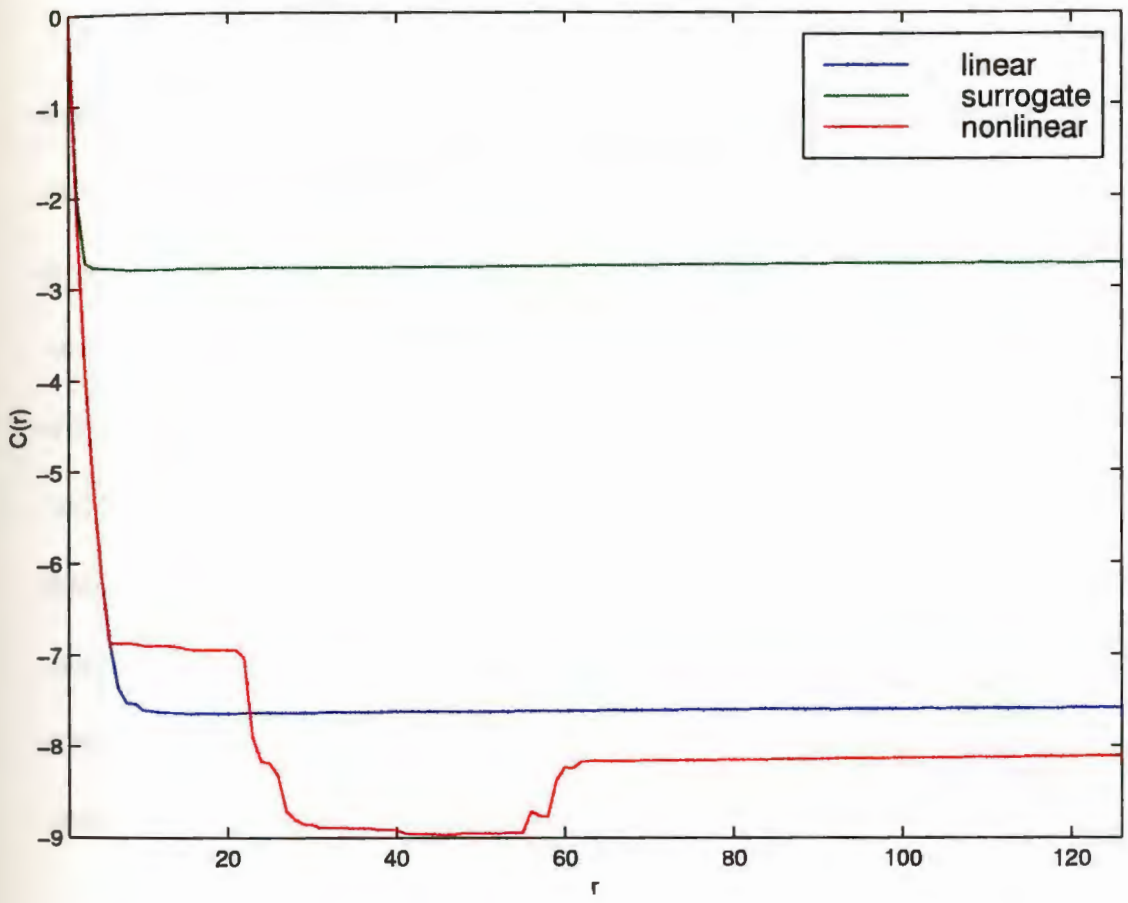

Figure 14: $C(r)$ plot for linear, surrogate-linear, and nonlinear mapping functions on the "daily" ($\delta t = 0.05$ months) Vallis model data set subsampled at 1 data point per 7 days. The parameter values used here are $\kappa = 5$ and $d = 4$.

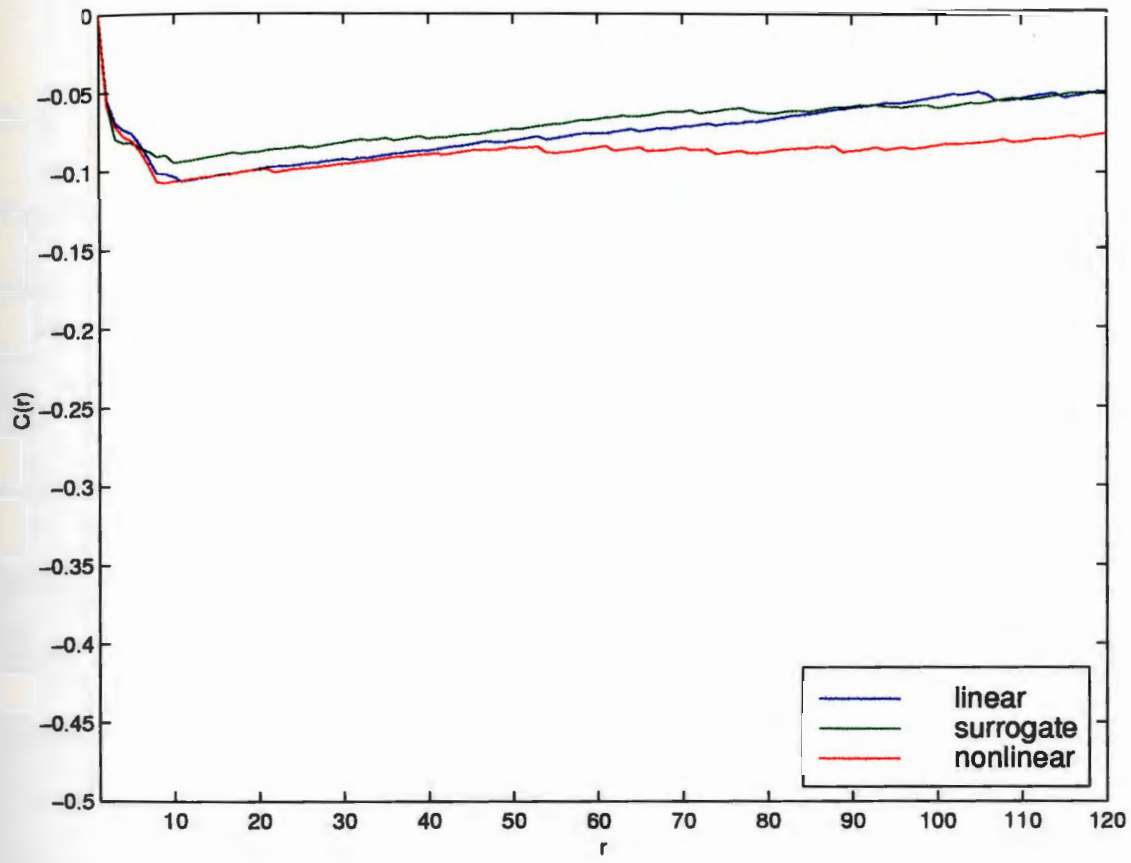

Figure 15: $C(r)$ plot for linear, surrogate-linear, and nonlinear mapping functions on the daily T-D (Tahiti minus Darwin sea-level-pressure) data set subsampled at 1 data point per 7 days. The parameter values used here are $\kappa = 7$ and $d = 3$.

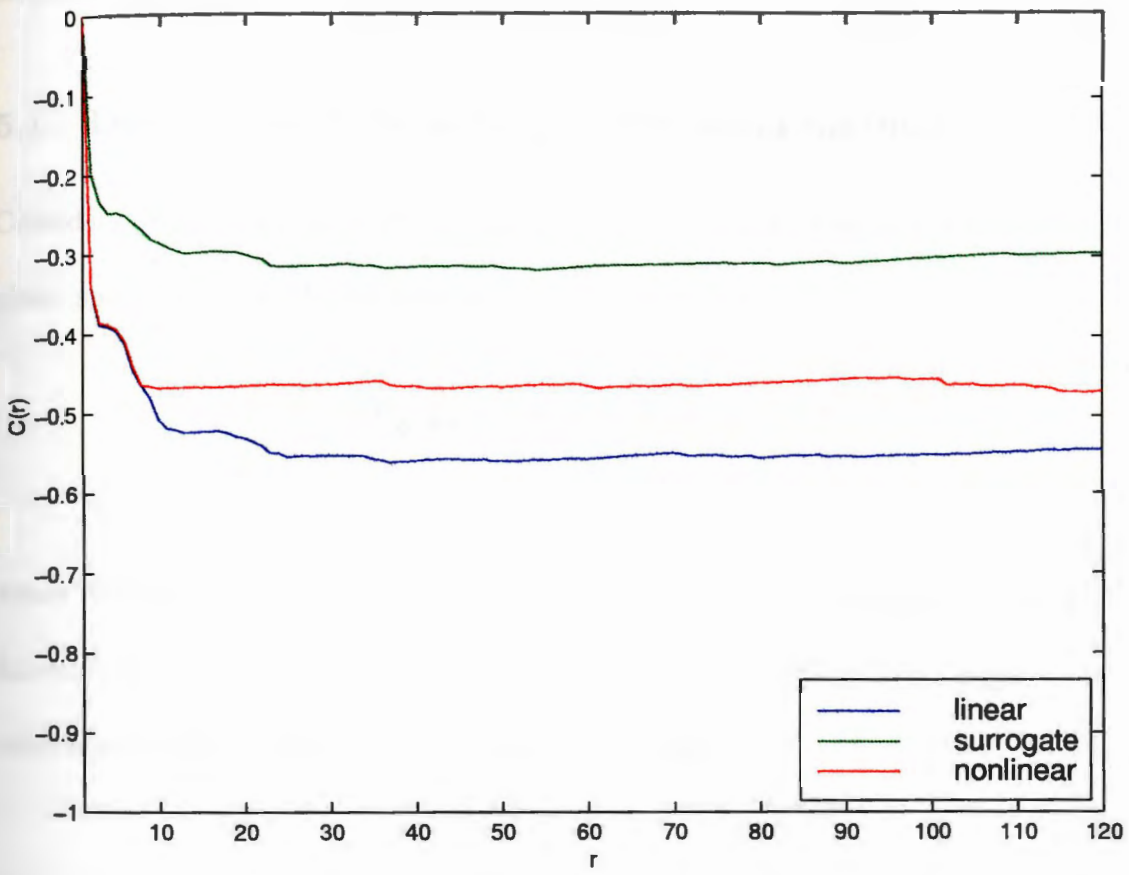

Figure 16: $C(r)$ plot for linear, surrogate-linear, and nonlinear mapping functions on the Darwin SLP data set subsampled at 1 data point per 14 days (bi-weekly). The parameter values used here are $\kappa = 7$ and $d = 3$.

5 Correlation Integrals

One of the earliest methods for characterizing a chaotic time series is the *Grassberger and Procaccia* [1986] method of calculating the correlation dimension, D_c, from the slope in log-log space of the correlation integral.

5.1 Description of Grassberger-Procaccia method

Consider a dynamical system with state vector, $\vec{X}$, which evolves in a d-dimensional phase space. The correlation integral, $C(l)$, is defined as

$$C(l) = \lim_{N\to\infty} \frac{1}{N^2} \times \{\text{number of pairs } (i,j) \text{ whose vector distance } |\vec{X}_i - \vec{X}_j| \text{ is less than } l\}, \quad (3)$$

where N is the number of vector pairs, $\vec{X}_i, \vec{X}_j$, used in the calculation. The distance function can be any vector norm; in this study I use the Euclidian norm unless otherwise specified. If

$$C(l) \sim l^{\nu}, \quad (4)$$

or equivalently $\log C(l) \sim \nu \log l$, then ν is called the correlation dimension, D_c. For instance, consider a line (a one-dimensional object), in an n-dimensional phase space. Equation 4 says that as the radius, l, of an n-dimensional hypersphere grows, the number of points encompassed by that hypersphere will grow as l^1.

When working with experimental data, one does not often have access to all of the components of the state vector, $\vec{X}$. Therefore, *Grassberger and Procaccia* [1986] suggest using the method of time-delay embedding to apply their method to time

series consisting of a single variable.

First one constructs a set of d-dimensional vectors from the original time series, $x(t)$ as follows:

$$\vec{\mathcal{X}}_i = (x(t_i), x(t_i + \tau), \ldots, x(t_i + (d-1)\tau)\,. \tag{5}$$

τ is a fixed time interval, and d needs to be larger than the attractor's dimension. Furthermore, for a bounded data set of non-infinite length, $C(l) \to 1$ as $l \to \infty$ (eventually, all the data are encompassed by a hypersphere of radius l). Also, if the time series is finite, there is some minimum distance between the embedded phase space vectors; thus for all l less than that minimum distance, $C(l) = 0$. So for real data sets, equation (4) only holds for a finite range of l values. This range of appropriate l values is referred to as the "scaling region".

For this work, I calculate correlation integral derivatives, $dC^{(d)}(l)/d\log l$, for embedding dimensions, d, ranging from 2 to 14. A 0.41 log-unit width box average is applied to smooth the correlation integral derivatives. The scaling region is determined to be the region, in $\log l$ space, where the correlation derivatives converge and are horizontal for large enough d. The derivative value in the scaling region is the correlation dimension, but the scaling region can be narrow.

5.2 Vallis Model

The Vallis model (as described in Section 3) is used to substantiate the correlation integral calculations on the data sets. Although a similarly long data set is unavailable for comparison, the "true" correlation dimension for the model is cal-

culated from 50,000 monthly sampled points. From the correlation derivative plot (Figure 17), one can see that for all embedding dimensions greater than 3, there is a small range of l values where the derivatives apparently converge to 3.16. Thus, the correlation dimension, D_c, of the seasonally forced Vallis model is approximately 3.16. At first this may seem unreasonable since there are only 3 independent phase variables in the model, and the correlation dimension is supposed to be a *lower* limit on the number of variables of the underlying physical system. However, the seasonal forcing introduces an explicit time dependence into the system, and so the effective number of phase variables is raised by one. Thus 3.16 is below the phase-space dimension of 4.

The next step is to find out what can be determined from the available data sets. From the analysis of a 788-point (monthly sampled) Vallis data set (Figure 18, left) you can indeed tell that the D_c is bounded below 4. Because these calculations can be sensitive to time averaging, a 788-point monthly-averaged (but not otherwise smoothed) Vallis model data set was constructed. The results are hardly affected by the averaging (Figure 18, right), so monthly averaging, similar to that done in calculating the SOI, does not significantly affect the algorithm. However, Figure 18 also shows that the D_c may be underpredicted in these cases. Note that the slopes appear to be about 2–3, rather than 3–4 as in Figure 17.

A twenty-times-monthly, "daily", Vallis model data set was generated to test the plausibility of doing correlation integral calculations on the daily T-D data (Figure 19). The apparent correlation dimension of the daily set is significantly lower than that of the monthly-sampled model data. Because this probably indicates an

oversampling problem, the calculation was repeated using a maximum norm in the integration instead of the Euclidian norm, as suggested by *Grassberger* [1986], but no improvement over the original calculation was found (Figure 20).

5.3 Noisy Vallis Data

To evaluate the effects of noise on the determination of the correlation dimension, various levels of normally distributed noise were added to the 788-point, monthly-sampled, Vallis data set. The correlation dimension calculation is inconclusive if the noise has a standard deviation over 10% of the signal standard deviation (Figure 21). Nevertheless, with 5-10% noise, the correlation integral slopes display weak convergence similar to the boundedness observed for the noise-free data (Figure 22).

5.4 SOI

There is a weak indication in Figure 23 that $D_c \approx 10$ for the SOI data. This indicates that the supposed climate attractor has a fractal dimension greater than or equal to 10, that the noise in the data is sufficiently large to destroy the convergence in the correlation integral calculation, or that the data set is too short to yield a reliable result. In any case, this result is consistent with the results from Section 4: the Southern Oscillation does not appear to be an example of low-dimensional chaos.

5.5 Daily T-D

For embedding dimensions higher than 11, the calculation indicates that the correlation dimension for the T-D data set is roughly 8.5 (Figure 24). The same D_c estimate is obtained using the maximum norm (Figure 25). However, in the light of the analysis on the Vallis model cited above (Figures 17, 19, and 20) this may be an underestimate due to oversampling.

5.6 Darwin SLP

Figure 26 shows the correlation integral slopes calculated from the Darwin SLP data set. These slopes seem to converge to a value between 6 and 6.5 for embedding dimensions between 7 and 14. As with the results for the T-D data set, this too may be an underestimate.

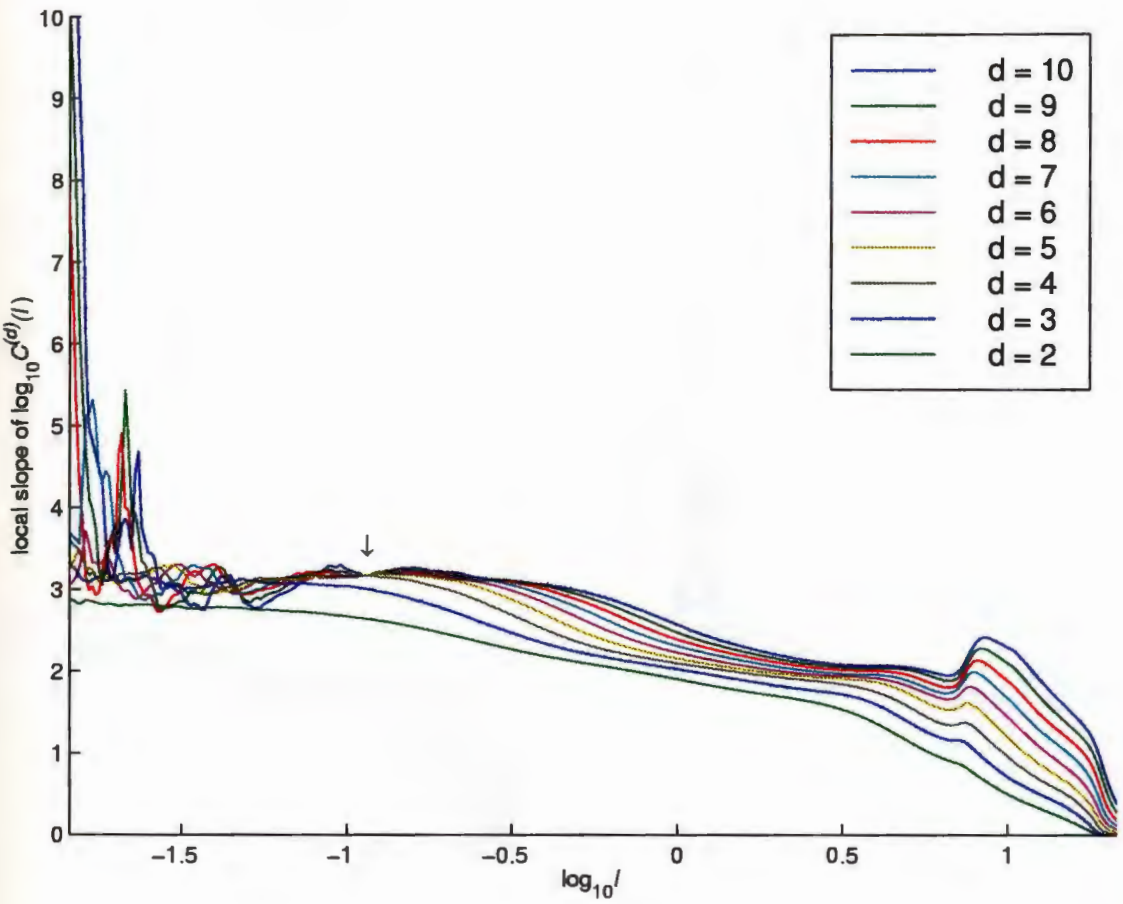

Figure 17: Correlation integral 5-point derivatives of the Vallis model for various embedding dimensions, d. The data set used consisted of 50,000 points of monthly sampled u values. The arrow points to the scaling region. Inspection of this plot reveals that the $D_c = 3.16$.

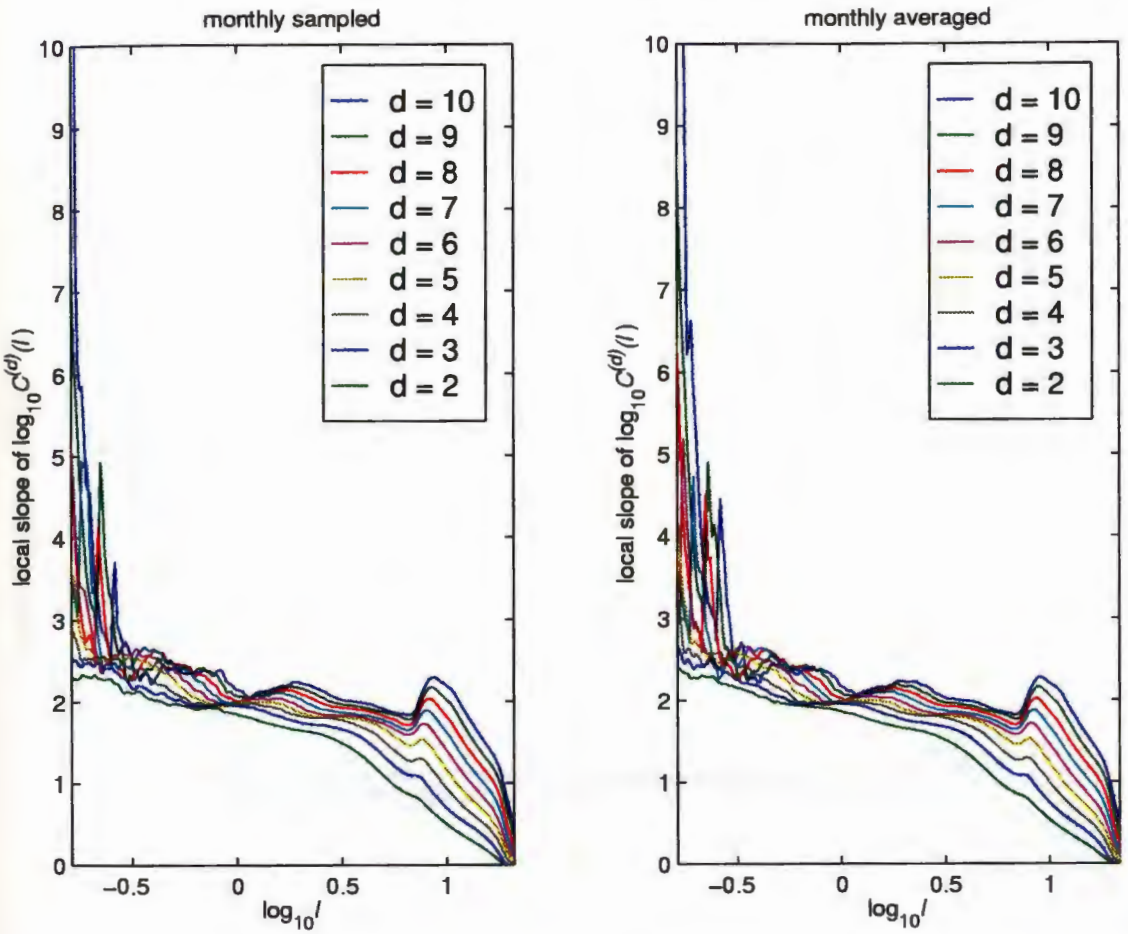

Figure 18: Correlation integral derivatives of Vallis model data.

Left: 788 points of monthly-sampled Vallis model u data.

Right: 788 points of monthly-averaged Vallis model u data. The monthly averages were computed from a data set sampled 20 times per month.

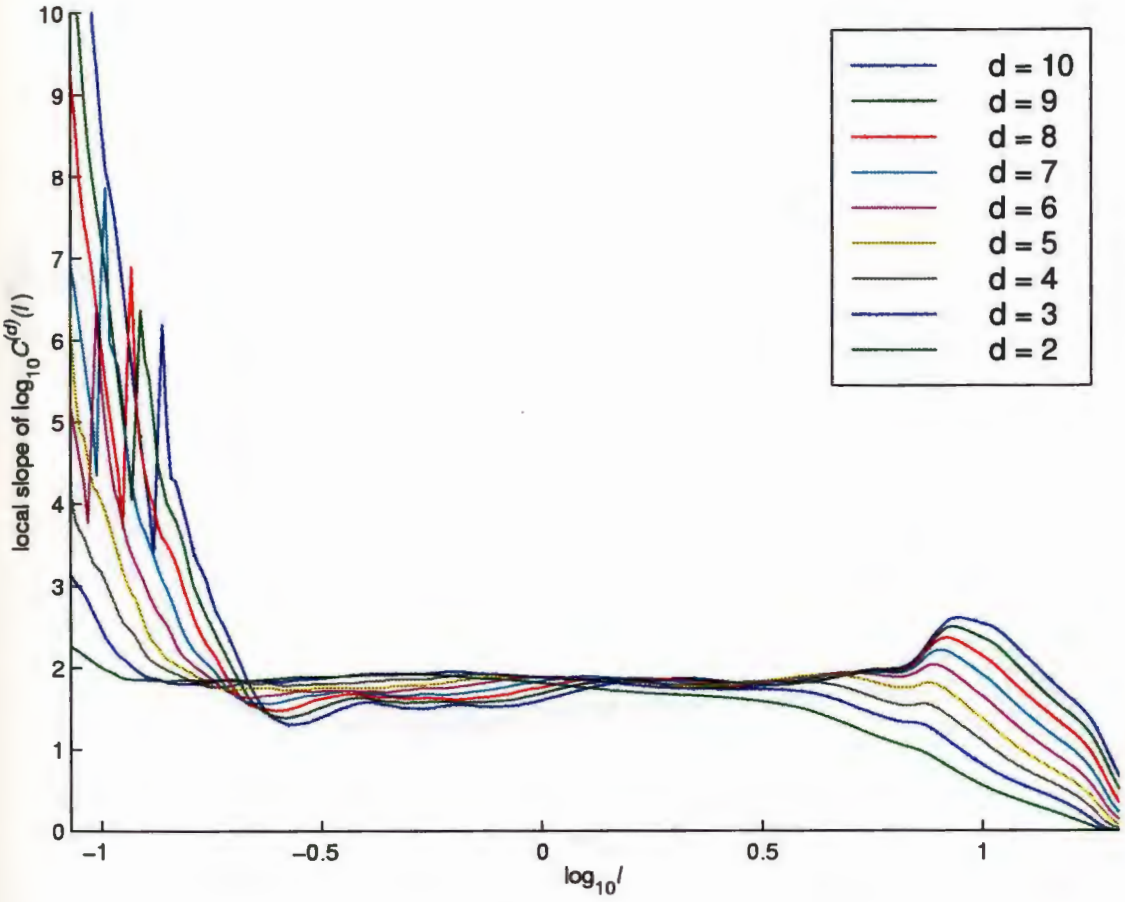

Figure 19: The same as Figure 17 except the data set used was 7557 points of u values sampled 20 times monthly.

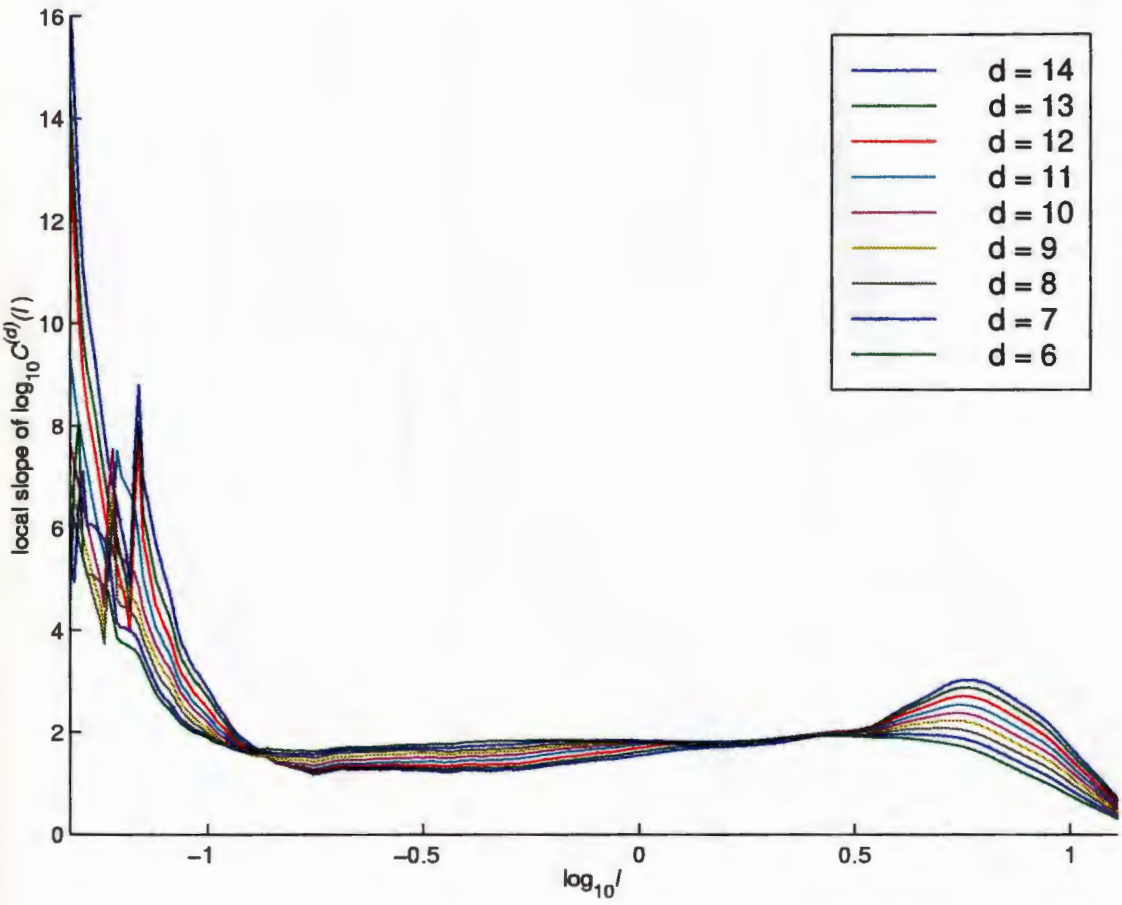

Figure 20: The same as Figure 17 except the data set used was 7557 points of u values sampled 20 times monthly. This calculation was done using a maximum norm rather than the standard Euclidian norm.

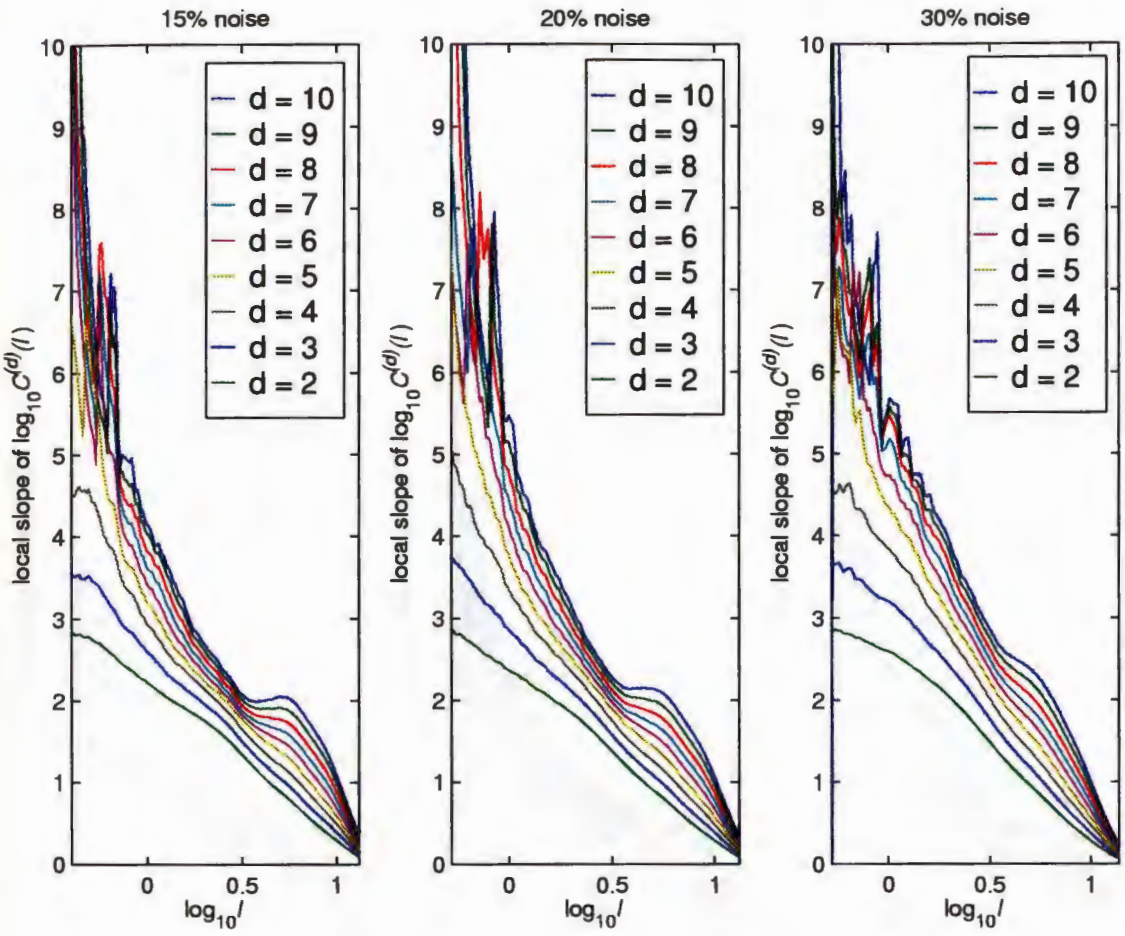

Figure 21: Correlation integral derivatives for the Vallis model with 788 points of monthly-sampled data computed using the maximum norm. The maximum norm was used here because it resulted in better convergence of the correlation integrals. Surrogate noise is added as shown.

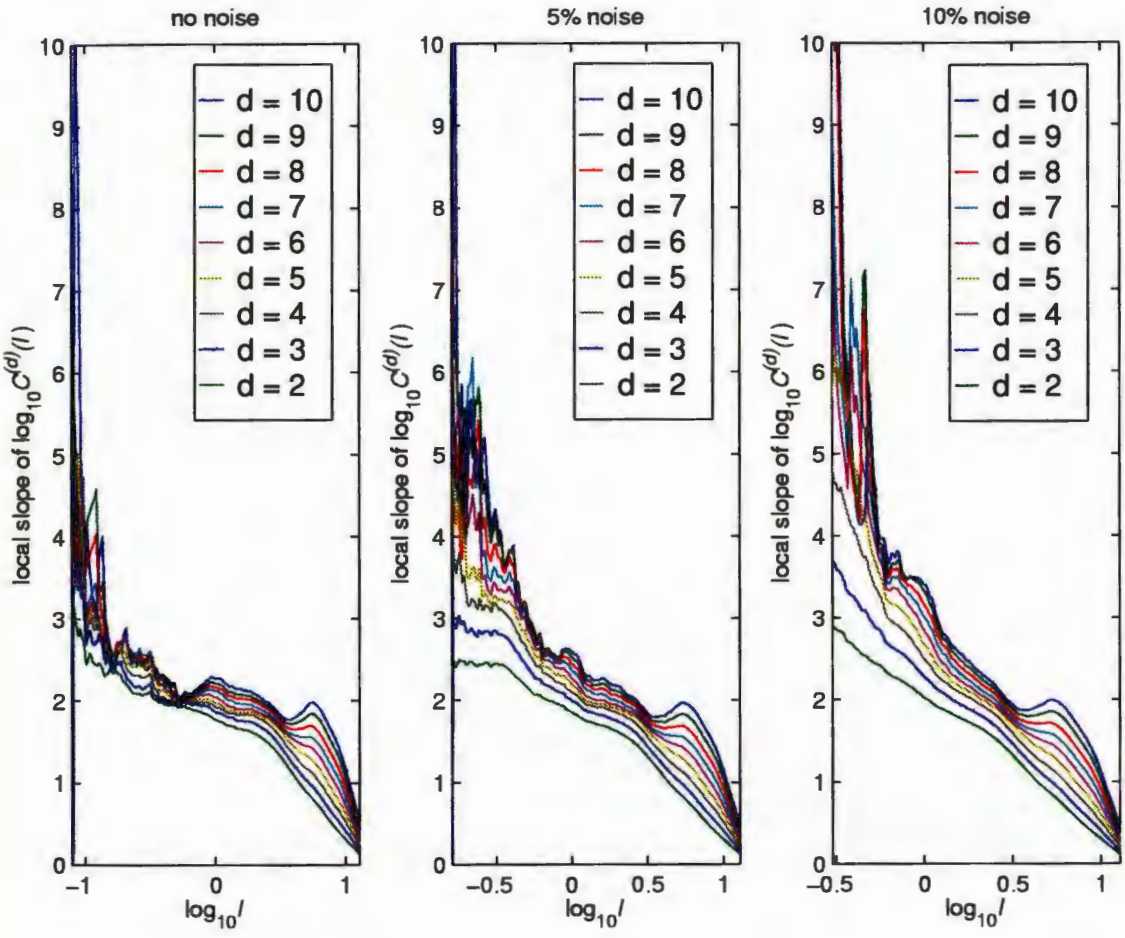

Figure 22: Same as Figure 21, but with less noise, as shown.

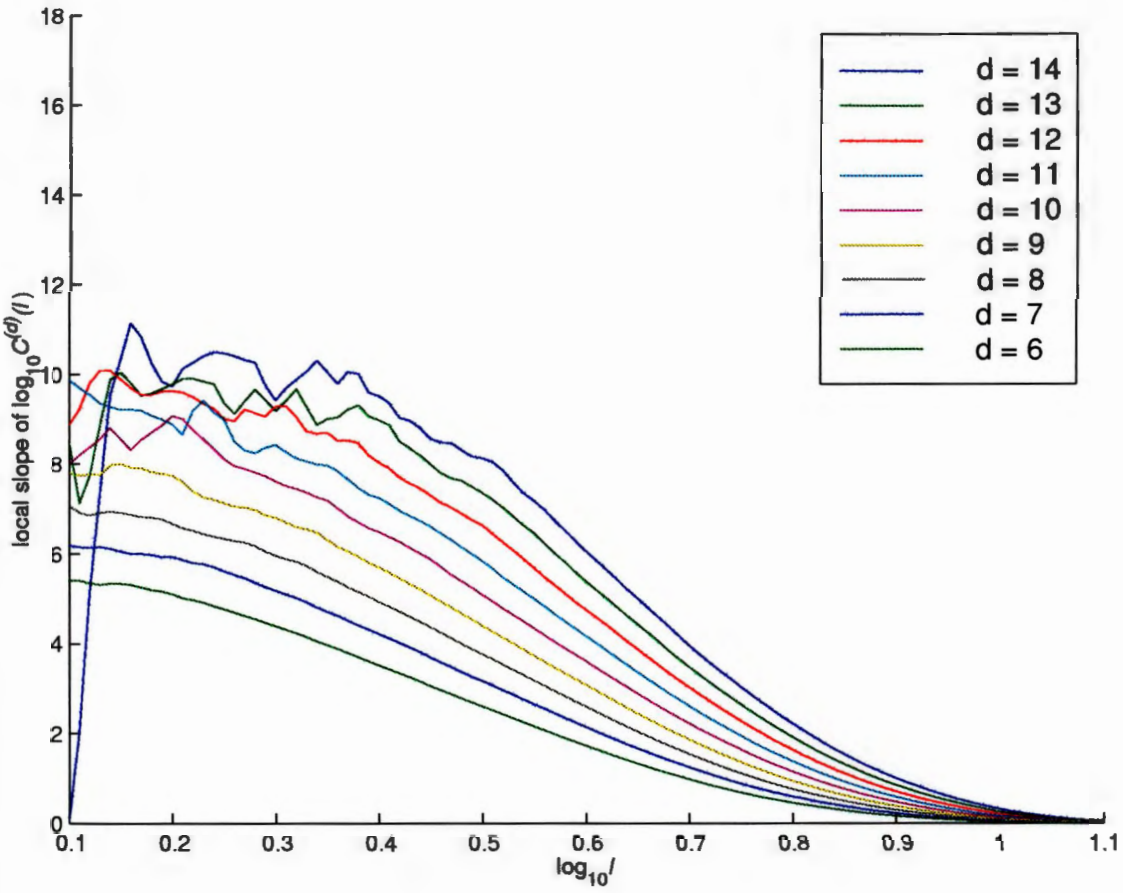

Figure 23: Correlation integral derivatives for the SOI data set.

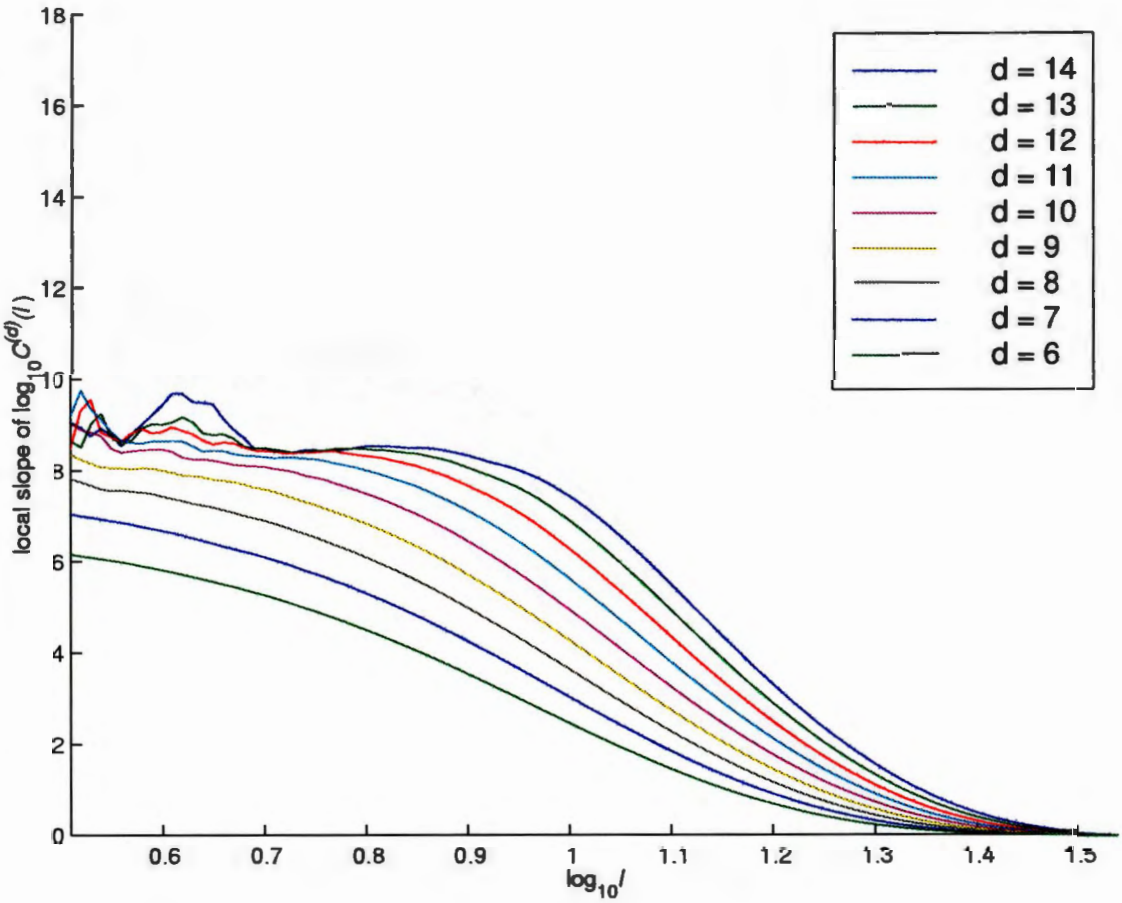

Figure 24: T-D correlation integral derivatives.

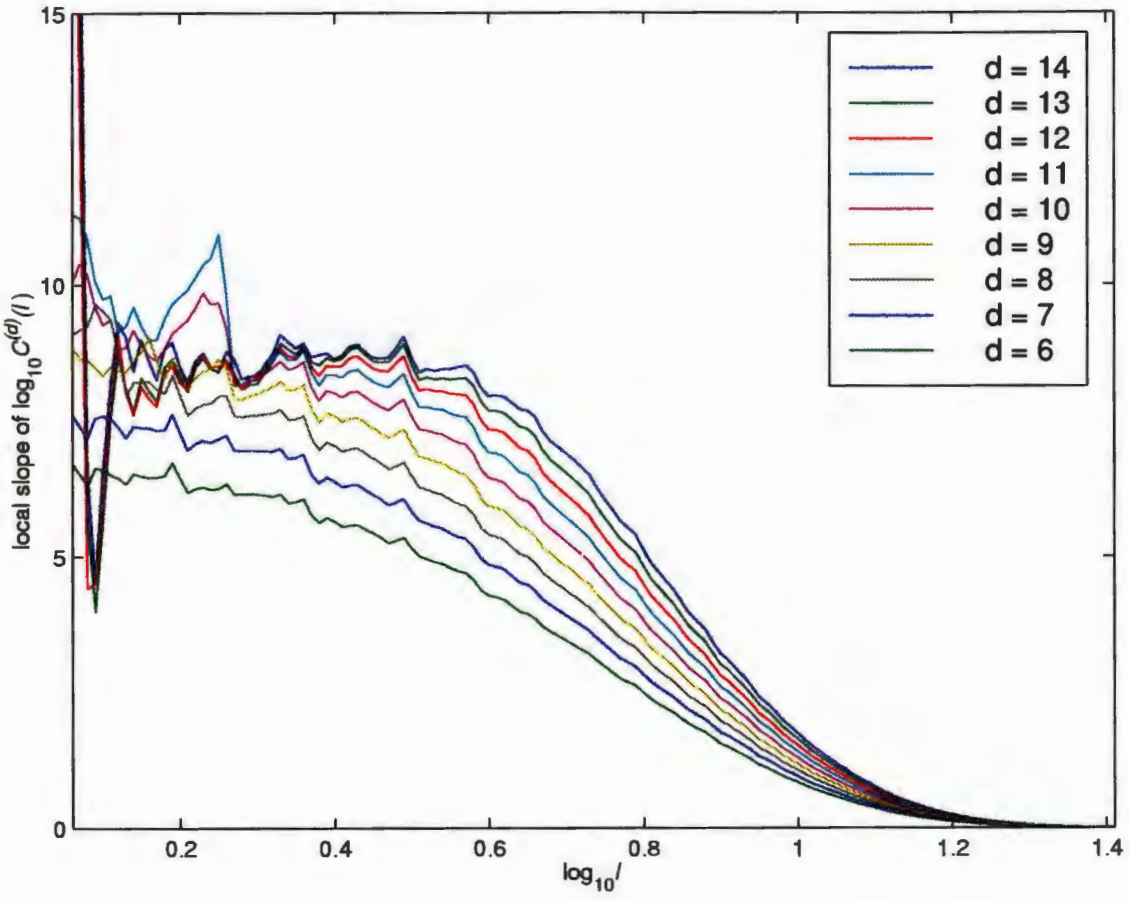

Figure 25: T-D correlation integral derivatives calculated using the maximum norm.

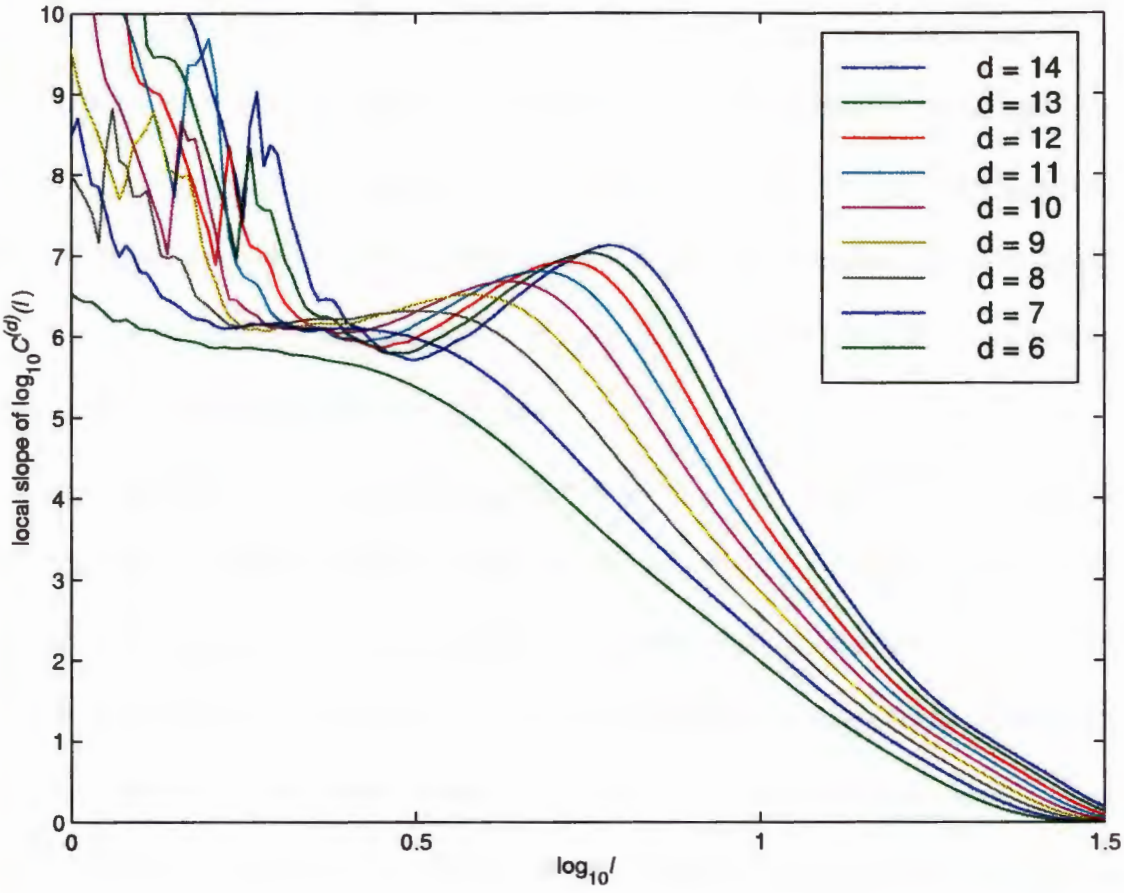

Figure 26: Darwin SLP correlation integral derivatives.

6 Synthesis and Conclusions

6.1 Synthesis

The arguments in Sections 4 and 5 rest on the assumptions that the SLP difference between Tahiti and Darwin is characteristic of the dynamics of the Southern Oscillation and that any measurement errors in the data sets have standard deviations which are small compared to the signal standard deviation. The results from the B/P and correlation integral analyses indicate one (or more) of two possibilities: the dynamics are not those of low-order nonlinear determinism, or localized physical processes (dynamic noise unrelated to ENSO) are obscuring an underlying large-scale, low-order nonlinear dynamics.

Section 4 shows that the B/P algorithm does not detect low-order nonlinear determinism in the SOI, Darwin SLP or T-D data sets. In interpreting this result the following facts need to be considered. (1) Nonlinear determinism is detectable by the algorithm in Vallis model data sets with lengths and time-sampling rate the same or similar to the observational data sets. Thus the data sets' lengths and sampling rates are not responsible for the null result. (2) The model's nonlinear determinism is apparent when the short time series is contaminated with additive noise having a standard deviation of up to 60% of the signal's standard deviation. Thus measurement errors, which are almost certainly less than 60% of the signal standard deviation, are not causing the nonlinear signal to be lost. (3) The B/P algorithm detected nonlinear determinism in a model data set which mimicked the monthly time-averaging of the SOI. Thus the SOI's time averaging is not masking

any nonlinear signal in the data. (4) Spatial averaging, such as that done in processing the T-D data set, should average out any signals from small-scale physical processes unrelated to the large-scale dynamics. The fact that nonlinear determinism is not detected in the T-D data set suggests that those small-scale processes are also not responsible for the null result.

Thus, the most likely conclusion to be drawn from the B/P analysis in Chapter 4 is that ENSO is not an example of low-order chaos. The short lengths of the data sets put computational limits on the size of κ, consequently the B/P analysis can only be used to discern low-order nonlinearity. For these data sets, $\kappa = 7$ seems to be the largest possible embedding dimension, so this result leaves open the possibility that ENSO is driven by mid- or high-order nonlinear dynamics.

Section 5 shows that the derivatives of the correlation integrals for the SOI and T-D data sets weakly indicate $D_c \approx 8 - 10$. This calculation is less immune to noise than the B/P calculations in Chapter 4: the model correlation integral derivatives only converge when less than about 10% noise is added. Furthermore, the model correlation integral derivatives apparently converge to D_c values which are less than the real model D_c, when the model data set has a length and sampling rate comparable those of the data sets. However, monthly averaging does not affect the model D_c calculations noticeably.

Assuming that measurement noise is not significant, the correlation integral calculations, nevertheless, place a lower bound on the number of dimensions in which ENSO evolves. Any false results here would be an *underestimate* of the real D_c, not an overestimate. Thus, it appears that the correlation dimension of the SOI

is at least eight, i.e., not "significantly less than 10". Taking this as our criterion for "low-order" chaos we conclude from Sections 4 and 5 that the SOI, and hence ENSO, cannot be usefully described as low-order chaos.

6.2 Conclusions about ENSO

If one accepts the idea presented here that ENSO is not low-order chaos, what ramifications does this have? Most simply, one can say that currently available chaos prediction techniques will not enhance our ability to predict ENSO events. The lack of low-order nonlinear determinism implies that the tropical Pacific Ocean and atmosphere processes responsible for ENSO are complicated. Any models for ENSO which exhibit low-order chaos are probably too simple to produce reliable, accurate predictions of ENSO episodes.

If daily Tahiti SLP data from the 1950's to the present could be obtained, they could be combined with the Darwin SLP data set to produce a nearly 17,000 term "daily Southern Oscillation Index". With such a long series it would be possible, in principle, to investigate the hypothesis that ENSO is governed by medium-order chaos by increasing κ in the B/P method to values in the range of 10–20.

A SOI source

For this research, the Southern Oscillation Index data set was obtained from the NOAA Climate Prediction Center in Washington DC through their web site at

`http://nic.fb4.noaa.gov:80/data/cddb/`

This data set was downloaded May 6, 1998. Two data files from the site were used in compiling the complete SOI data set; these are "`soi`" and "`soi.his`".

(STAND TAHITI - STAND DARWIN) SEA LEVEL PRESS STANDARDIZED DATA												
Year	Jan	Feb	Mar	Apr	May	Jun	Jul	Aug	Sep	Oct	Nov	Dec
1932	-	-	-	-	-	-	-	-	-1.1	-0.6	-0.6	0.2
1933	-1.6	0.4	-0.4	0.3	0.5	-0.4	0.2	-0.2	0.3	0.2	0.5	0.9
1934	0.7	0.0	-0.1	0.4	-0.5	0.8	0.2	-2.5	-0.7	0.3	1.1	-0.4
1935	0.8	-0.7	1.3	0.3	-0.4	-0.2	0.0	0.1	0.6	0.7	0.2	-0.6
1936	-0.3	-0.1	0.0	0.5	0.4	-0.3	0.3	-1.0	0.2	-0.1	-1.5	-0.1
1937	1.1	-0.8	0.6	0.1	-0.1	0.1	-0.5	0.1	0.1	-0.5	-0.5	0.6
1938	0.8	0.4	-0.5	0.3	1.0	1.3	1.8	1.0	0.9	1.3	0.0	1.6
1939	2.1	0.8	1.1	0.7	-0.1	-0.2	0.8	-0.3	-1.1	-1.7	-1.0	-1.2
1940	-0.1	-0.8	-1.3	-0.7	-1.2	-1.7	-1.6	-1.9	-2.0	-1.9	-0.9	-2.6
1941	-1.4	-2.2	-1.4	-0.9	-0.6	-1.2	-2.0	-2.0	-0.9	-2.2	-1.1	-1.2
1942	-1.8	-0.7	-0.8	-0.4	0.4	0.5	-0.2	0.2	0.9	0.7	-0.6	1.6
1943	1.2	1.2	0.3	1.0	0.2	-0.7	0.2	0.6	0.5	0.8	0.2	-1.2
1944	-1.2	0.4	0.5	-0.4	-0.1	-0.4	-0.9	0.2	0.3	-1.0	-0.8	0.3
1945	0.6	0.7	1.4	-0.5	0.0	0.5	0.3	1.0	0.9	0.1	-0.5	0.7
1946	-0.4	0.4	-0.4	-0.7	-0.9	-0.9	-1.1	-0.6	-1.8	-1.4	-0.3	-0.9
1947	-0.7	-0.8	1.2	-0.4	-1.1	0.1	0.9	0.5	1.2	-0.3	0.7	0.5
1948	-0.5	-0.5	-0.7	0.2	0.3	-0.5	0.0	-0.6	-0.9	0.5	0.2	-0.9
1949	-1.1	0.1	0.5	0.1	-0.5	-1.0	-0.2	-0.6	0.2	0.4	-0.8	0.7
1950	0.5	2.1	1.9	1.2	0.6	2.0	2.0	1.1	0.7	1.6	1.0	2.7
1951	1.7	0.6	-0.8	-0.6	-1.0	-0.3	-1.4	-0.7	-1.3	-1.4	-1.0	-1.0
1952	-1.2	-1.1	0.0	-0.5	0.6	0.5	0.4	-0.4	-0.3	0.2	-0.2	-1.6
1953	0.2	-1.0	-0.8	-0.1	-2.2	-0.3	-0.1	-1.9	-1.5	-0.2	-0.4	-0.7
1954	0.6	-0.7	-0.3	0.4	0.3	-0.3	0.3	0.8	0.2	0.1	0.1	1.5
1955	-0.7	1.8	0.1	-0.5	0.9	1.1	1.7	1.2	1.5	1.5	1.3	1.0

Year	Jan	Feb	Mar	Apr	May	Jun	Jul	Aug	Sep	Oct	Nov	Dec
1956	1.4	1.5	0.9	0.7	1.3	0.8	1.1	0.9	0.0	1.9	0.1	1.0
1957	0.6	-0.5	-0.4	0.0	-1.0	-0.2	0.1	-1.0	-1.1	-0.2	-1.2	-0.5
1958	-2.3	-1.0	-0.3	0.1	-0.9	-0.2	0.3	0.6	-0.4	-0.2	-0.6	-0.9
1959	-1.2	-2.0	0.9	0.2	0.3	-0.6	-0.5	-0.6	0.0	0.3	1.0	0.8
1960	0.0	-0.3	0.6	0.6	0.3	-0.3	0.4	0.5	0.7	-0.1	0.5	0.8
1961	-0.4	0.7	-2.7	0.7	0.1	-0.3	0.1	-0.2	0.1	-0.7	0.6	1.6
1962	2.2	-0.7	-0.4	0.0	1.0	0.4	-0.1	0.3	0.5	0.9	0.3	0.0
1963	1.1	0.4	0.7	0.6	0.1	-1.0	-0.3	-0.5	-0.7	-1.6	-1.0	-1.6
1964	-0.5	-0.3	0.7	1.0	-0.1	0.4	0.4	1.3	1.4	1.3	0.0	-0.5
1965	-0.6	0.1	0.2	-0.8	-0.1	-1.0	-2.2	-1.2	-1.5	-1.2	-1.8	0.0
1966	-1.7	-0.7	-1.7	-0.5	-0.7	0.0	-0.1	0.3	-0.3	-0.4	-0.1	-0.6
1967	1.9	1.6	0.8	-0.3	-0.3	0.3	0.0	0.5	0.6	-0.2	-0.6	-0.8
1968	0.4	1.1	-0.5	-0.2	1.1	0.9	0.6	-0.1	-0.3	-0.3	-0.5	0.0
1969	-2.0	-1.1	-0.1	-0.6	-0.6	-0.2	-0.7	-0.6	-1.2	-1.3	-0.2	0.3
1970	-1.4	-1.6	0.0	-0.4	0.1	0.7	-0.6	0.2	1.3	0.9	1.7	2.1
1971	0.3	1.9	2.1	1.7	0.7	0.1	0.1	1.3	1.6	1.7	0.5	0.0
1972	0.4	0.8	0.1	-0.4	-2.1	-1.1	-1.9	-1.0	-1.6	-1.2	-0.5	-1.6
1973	-0.5	-2.0	0.2	-0.2	0.2	0.8	0.5	1.1	1.4	0.6	2.9	2.0
1974	2.7	2.0	2.2	0.8	0.9	0.1	1.2	0.5	1.3	0.8	-0.3	0.0
1975	-0.8	0.6	1.2	1.1	0.5	1.1	2.1	1.9	2.4	1.7	1.3	2.3
1976	1.5	1.6	1.3	0.1	0.2	-0.1	-1.2	-1.3	-1.4	0.2	0.7	-0.6
1977	-0.7	1.1	-1.3	-0.8	-0.9	-1.5	-1.5	-1.3	-1.0	-1.4	-1.6	-1.4
1978	-0.4	-3.5	-0.8	-0.6	1.3	0.3	0.4	0.0	0.0	-0.7	-0.1	-0.3
1979	-0.7	0.8	-0.5	-0.4	0.3	0.4	1.3	-0.6	0.1	-0.4	-0.6	-1.0
1980	0.3	0.0	-1.2	-1.0	-0.3	-0.4	-0.2	0.0	-0.6	-0.3	-0.5	-0.3
1981	0.2	-0.6	-2.1	-0.4	0.7	1.0	0.8	0.4	0.4	-0.7	0.1	0.5
1982	1.3	-0.1	0.1	-0.2	-0.7	-1.6	-1.9	-2.5	-2.0	-2.2	-3.2	-2.8
1983	-4.2	-4.6	-3.4	-1.3	0.5	-0.3	-0.8	-0.2	1.0	0.3	-0.2	-0.1
1984	0.1	0.6	-0.9	0.2	0.0	-0.8	0.0	0.0	0.1	-0.6	0.2	-0.4
1985	-0.5	1.0	0.2	1.0	0.2	-0.9	-0.3	0.7	0.0	-0.7	-0.3	0.1
1986	0.9	-1.6	0.0	0.1	-0.5	0.7	0.1	-1.0	-0.6	0.5	-1.5	-1.8
1987	-0.9	-1.9	-2.0	-1.9	-1.7	-1.7	-1.7	-1.5	-1.2	-0.7	-0.1	-0.7
1988	-0.2	-0.9	0.1	-0.1	0.8	-0.2	1.1	1.4	2.1	1.4	1.9	1.3
1989	1.7	1.1	0.6	1.6	1.2	0.5	0.8	-0.8	0.6	0.6	-0.4	-0.7
1990	-0.2	-2.4	-1.2	0.0	1.1	0.0	0.5	-0.6	-0.8	0.1	-0.7	-0.5
1991	0.6	-0.1	-1.4	-1.0	-1.5	-0.5	-0.2	-0.9	-1.8	-1.5	-0.8	-2.3
1992	-3.4	-1.4	-3.0	-1.4	0.0	-1.2	-0.8	0.0	0.0	-1.9	-0.9	-0.9
1993	-1.2	-1.3	-1.1	-1.6	-0.6	-1.4	-1.1	-1.5	-0.8	-1.5	-0.2	0.0
1994	-0.3	-0.1	-1.4	-1.8	-1.0	-0.9	-1.8	-1.8	-1.8	-1.6	-0.7	-1.6
1995	-0.6	-0.5	0.2	-1.1	-0.7	-0.2	0.3	-0.1	0.3	-0.3	0.0	-0.8
1996	1.0	-0.1	0.7	0.6	0.1	1.0	0.6	0.4	0.6	0.4	-0.2	0.8
1997	0.5	1.6	-1.1	-0.9	-1.8	-2.0	-1.0	-2.1	-1.6	-1.9	-1.4	-1.3
1998	-3.3	-2.7	-3.4	-1.9	-	-	-	-	-	-	-	-

Bibliography

Abarbanel, H. D. I., *Analysis of Observed Chaotic Data.* Springer-Verlag, New York, 1996.

Barahona, M., and C. Poon, Detection of nonlinear dynamics in short, noisy time series, *Letters to Nature.* **381**, 215–217, 1996.

Bauer, S. T., and M. G. Brown, Empirical low-order ENSO dynamics, *Geophysical Research Letters.* **19**, 2055–2058, 1992.

CPC (Climate Prediction Center, NOAA), *Experimental Long-Lead Forecast Bulletin.* **6**, No. 1, March, 1992.

Elsner, J. B., and A. A. Tsonis, Nonlinear dynamics established in the ENSO, *Geophysical Research Letters.* **20**, 213–216, 1993.

Grassberger, P., Do climate attractors exist? *Nature.* **323**, 609–612, 1986.

Grassberger, P., and I. Procaccia, Measuring the strangeness of strange attractors *Physica D.* **9**, 189-208, 1983.

Grassberger, P. and I. Procaccia, Characterization of experimental (noisy) strange attractors, *Physical Review A.* **29**, 975-977.

Hense, A., On the possible existence of a strange attractor for the Southern Oscillation, *Beiträge zur Physik der Atmosphäre.* **60**, 34–47, 1987.

Hilborn, R. C., *Chaos and Nonlinear Dynamics.* Oxford University Press, New York, 1994.

Jin, F., J. D. Neelin, and M. Ghil, El Niño on the devil's staircase: Annual subharmonic steps to chaos, *Science.* **264**, 70–74, 1994.

Lorenz, E. N., Deterministic nonperiodic flow, *Journal of the Atmospheric Sciences.* **20**, 130–141, 1963.

Münnich, M., M. A. Cane, and S. Zebiak, A study of self-excited oscillations of the tropical ocean-atmosphere system. Part II: Nonlinear cases, *Journal of the Atmospheric Sciences.* **48**, 1238–1248, 1991.

Philander, S. G., *El Niño, La Niña, and the Southern Oscillation.* Academic Press, San Diego, 1990.

Quinn, W. H., V. T. Neal, and S. E. A. de Mayolo, El Niño occurrences over the past four and a half centuries, *Journal of Geophysical Research.* **92**, 14,449–14,461, 1987.

Seaman, R., W. Bourke, P. Steinle, T. Hart, G. Embery, M. Naughton, and L. Rikus, Evolution of the Bureau of Meteorology's Global Assimilation and Prediction system. Part 1: analysis and initialisation. *Australian Meteorological Magazine*, **44**, 1-18, 1995.

Tziperman, E., M. A. Cane, and S. E. Zebiak, Irregularity and locking to the seasonal cycle in an ENSO prediction model as explained by the quasi-periodic route to chaos, *Journal of the Atmospheric Sciences.* **52**, 293–306, 1995.

Walters, G., *Australian Southern Hemisphere Tropical Analysis, Daily 1972 April-continuous.* [NCAR tape archive ds108.0], National Center for Atmospheric Research, Boulder, Colorado, 1997.

Vallis, G. K., El Niño: A chaotic dynamical system? *Science.* **232**, 243–245, 1986.

Vallis, G. K., Conceptual models of El Niño and the Southern Oscillation, *Journal of Geophysical Research.* **93**, 13,979–13,991, 1988.